Identifiability of soft tissue constitutive parameters from *in-vivo* macro-indentation

Zohar Oddes [a] and Dana Solav [a,*]

a. Faculty of Mechanical Engineering, Technion Institute of Technology, Haifa, Israel
* Corresponding author: danas@technion.ac.il

Abstract

Reliable identification of soft tissue material parameters is frequently required in a variety of applications, particularly for biomechanical simulations using finite element analysis (FEA). However, determining representative constitutive laws and material parameters is challenging and often comprises a bottleneck that hinders the successful implementation of FEA. Soft tissues exhibit a nonlinear response and are commonly modeled using hyperelastic constitutive laws. *In-vivo* material parameter identification, for which standard mechanical tests (e.g., uniaxial tension and compression) are inapplicable, is commonly achieved using finite macro-indentation test. Due to the lack of analytical solutions, the parameters are commonly identified using inverse FEA (iFEA), in which simulated results and experimental data are iteratively compared. However, determining what data must be collected to accurately identify a *unique* parameter set remains unclear. This work investigates the sensitivities of two types of measurements: indentation force-depth data (e.g., measured using an instrumented indenter) and full-field surface displacements (e.g., using digital image correlation). To eliminate model fidelity and measurement-related errors, we employed an axisymmetric indentation FE model to produce synthetic data for four 2-parameter hyperelastic constitutive laws: compressible Neo-Hookean, and nearly incompressible Mooney-Rivlin, Ogden, and Ogden-Moerman models. For each constitutive law, we computed the objective functions representing the discrepancies in the reaction force, the surface displacement, and their combination, and visualized them for hundreds of parameter sets, spanning a representative range as found in the literature for the bulk soft tissue complex in human lower limbs. Moreover, we quantified three identifiability metrics, which provided insights into the uniqueness (or lack thereof) and the sensitivities. This approach provides a clear and systematic evaluation of the parameter identifiability, which is independent of the selection of the optimization algorithm and initial guesses required in iFEA. Our analysis indicated that the indenter's force-depth data, despite being commonly used for parameter identification, was insufficient for reliably and accurately identifying both parameters for all the investigated material models and that the surface displacement data improved the parameter identifiability in all cases, although the Mooney-Rivlin parameters remained poorly identifiable. Informed by the results, we then discuss several identification strategies for each constitutive model. Finally, we openly provide the codes used in this study, to allow others to further investigate the indentation problem according to their specifications (e.g., by modifying the geometries, dimensions, mesh, material models, boundary conditions, contact parameters, or objective functions).

Keywords: finite element analysis; soft tissue hyperelastic properties; uniqueness of material parameters;

1. Introduction

Soft biological tissues exhibit a broad range of characteristic mechanical behaviors, such as nonlinear, anisotropic, and strain-rate dependent responses, which are attributed to their distinct biological microstructures [1]. Accordingly, the bulk mechanical response of the soft tissue complex to external loads exhibits similar traits and is fundamentally specific to both the anatomical region and the individual. Consequently, many applications in which the mechanical response of soft tissues plays a major role must account for this inter- and intra-subject variability. Modern computational tools, such as patient-specific finite element analysis (FEA), are commonly and increasingly used to simulate the mechanical behavior of a soft tissue complex under various loads, or to evaluate the effects of their interaction with medical devices, for various applications (e.g., surgical planning and computer-assisted surgery [2]–[7], investigation and diagnosis of diseases and injuries [8]–[12], and the design and evaluation of prostheses [13]–[15], orthoses [16], braces [17], footwear [18], [19], and compression garments [20], [21]. For example, patient-specific biomechanical models representing the residual limb of a lower limb amputee have been used to study and predict the effects of the mechanical interaction at the interface between the prosthetic socket and the biological limb, under various loading scenarios [13]. These FEA could then be used to numerically evaluate the performances of various designs [14], [22], [23] and to devise an FEA-based computational optimal design framework [24]. However, the reliability of such predictions and thus the effectiveness of the resulting design strongly rely on using a realistic constitutive law with appropriate material parameters for the patient's soft tissues [13], [23].

Patient-specific soft-tissue constitutive modeling and parameter calibration is considered a very challenging task for two main reasons: (1) for a complete description of the tissue mechanics, a large number of constitutive parameters must be identified; and (2) the patient-specific parameters must be identified *in-vivo*, deeming most standard mechanical tests invalid.

Consequently, quantifying patient-specific soft tissue material parameters remains a fundamental bottleneck that often hinders the successful implementation of these models.

Characterization of soft tissue mechanical properties typically involves carrying out any of several standard mechanical tests (e.g., uniaxial or biaxial tension, or compression) on excised tissue specimens *ex-vivo*. These tests were designed to allow sufficient control over the boundary conditions (BC) and produce some homogenous deformation in the specimen, for which an analytical solution exists. The material parameters are then identified by fitting the experimental data to the analytical model, based on the selected constitutive law [25]. Surveying the literature for soft tissue material parameters estimated in different studies across and among individuals reveals large variability, spanning up to four orders of magnitude [13], [26]. Many studies used parameter values obtained from animal specimens or human cadavers, despite mounting evidence that tissue properties are patient-specific [27] and that variations in constitutive models and parameter values may significantly impact the predicted stresses and strains [18], [23], which are associated with tissue damage and injury risk [28]. While *ex-vivo* tests are essential to understand the tissues' mechanical behavior and devise constitutive models to describe them, they are inapplicable for many clinical applications due to their invasiveness. Therefore, developing methods for estimating *in-vivo* tissue parameters remains a priority.

In-vivo investigations are challenging because applying homogeneous deformations on isolated tissues becomes inapplicable, and accurately determining the BCs is often difficult. To date, *in-vivo* attempts to identify the patient-specific soft tissue parameters have focused mainly on two methods: 1) suction/aspiration, e.g., for investigating the skin [10], [29], breast tissues [30], tongue [31], and various internal organs [9], [32], and 2) macro-indentation, e.g., for studying the soft tissues in the human thigh [20], [33], [34] shank [26], [35], foot [36]–[39], forearm skin [40]–[42], liver [43], and porcine brain [44]–[46]). The majority of indentation studies have analyzed the indenter's force-depth data. However, the extraction of material parameters from such data is not straightforward. The classical indentation model proposed by Hertz assumes that the indentation depth is infinitesimal compared to the sample, and is unsuitable for the large deformations associated with finite indentation of soft tissue [47]. Several studies have further developed analytical solutions for various conditions (e.g., [48]). Hayes et al. employed an analytical solution to the problem of axisymmetric indentation for testing the articular cartilage [49]. However, their formula was developed for thin layers lying on a rigid support and is limited to certain relations between the indenter's geometry, tissue thickness, and indentation depth, which may be incompatible with soft tissue regions of interest. Moreover, it only allows the extraction of an effective Young's modulus based on linear elasticity, whereas it is widely accepted that soft tissues exhibit highly nonlinear behavior. Finite macro-indentation of hyperelastic solids involves coupled material and geometric nonlinearities. Consequently, later studies focused on explicit empirical load-displacement relationships for hyperelastic materials based on FE simulations (e.g., [50]) and on inverse approaches, such as inverse FEA (iFEA, also known as FE model updating (FEMU)), to estimate material parameters from indentation tests (e.g., [20], [33], [35], [37], [51], [52]). In these procedures, a numerical model of the body part is created and the tissues are given constitutive parameters that are not limited to linear elasticity. To obtain the parameter values, iterative optimization algorithms are employed, whereby the parameter values are updated in each iteration based on an objective function representing the discrepancies between simulated and experimental results. This process is repeated until the objective function converges to a minimum value. At this point, the parameter set is said to be identified.

In some iFEA studies, the procedure is driven by a simplified FE model crudely representing the indented anatomical region based on assumed or measured dimensions (e.g., [26], [33]). Other, more complex procedures, integrated patient-specific geometrical models constructed from imaging data (e.g., [20], [35]). Rather than determining the individual mechanical properties of each soft tissue layer simultaneously (which may be problematic for the reasons discussed in the next paragraph), the bulk soft-tissue complex has often been represented as a lumped model of one, two, or three distinguishable homogenous regions [27], [33], [35], [53]. In numerous *in-vivo* indentation tests, only the indenter's force and depth were measured. However, extracting material parameters from the indenter's force-depth responses represents an inverse problem, which might be ill-posed. This implies that different parameter sets might exhibit equally good agreement between simulated and experimental data, even though only one set (or none) is the correct one. This problem, known as the *uniqueness* or *identifiability* problem, has been widely discussed, particularly in the context of soft tissues [12], [25], [54]–[59]. Nevertheless, most indentation studies did not report whether they evaluated the uniqueness of the identified parameters (e.g., by initializing the optimization procedure from multiple initial guesses) or even which parameter set they used as the initial guess, therefore, it is difficult to assess their validity. To date, the conditions for reliably identifying unique hyperelastic parameters from finite macro-indentation tests remain unclear.

It is generally agreed that the identifiability can be improved by increasing the amount and/or variety of experimental data. For example, measuring the full-field surface displacements using optical methods, such as digital image correlation (DIC), is becoming a common practice, particularly for tissue mechanical characterization [60], [61]. For non-flat bodies or out-of-plane displacement, three-dimensional DIC (3D-DIC) is required, utilizing multiple views to reconstruct the 3D surface of the body with up to 360˚ coverage, to compute the displacements of material points, and derive the local 3D deformations [62]–[64]. Although using 3D-DIC during indentations for soft tissue material parameter identification has been described over a decade ago [65], it has not been widely adopted, and the contribution of 3D-DIC data to parameter identifiability from indentations has not been explored. Specifically, it is still not clear which experimental quantities need to be measured to achieve convergence to a unique solution, and what are the sensitivities of each measurement to each material parameter.

Previous studies have utilized various measurement modalities during indentation to increase the variety of experimental data. One notable approach involves indentation using an instrumented ultrasound transducer for measuring the distance between the skin surface and the bone or other underlying tissue layers, potentially allowing the characterization of multiple

tissue layers. This clinically feasible and relatively inexpensive tool simultaneously measures the indentation force and the depth of each tissue layer. Early efforts have been reported by [27] and later also by several others [20], [33], [66], [67]. Moreover, ultrasound elastography has been utilized, to add information about the tissue stiffness [67]–[69]. Another approach for measuring the deformation of internal tissue layer consists of indentation inside an MRI scanner [36], [40], [70]. Both approaches are out of the scope of the present study, but can be further explored by adapting the provided open-source codes.

In the present study, we investigate the parameter identifiability with respect to two measurement modalities: indentation forces and full-field surface displacements. We consider a simplified axisymmetric indentation test carried on a cylindrical specimen with a homogeneous isotropic hyperelastic material. A generic FE model of the indentation problem is used to assess the identifiability of four commonly used two-parameter hyperelastic constitutive laws. To eliminate model fidelity and measurement-related errors, the same FE model is used for generating synthetic test data. For each constitutive law, the objective function is evaluated and visualized for hundreds of parameter sets, spanning a representative range as found in the literature for the bulk soft tissue complex in human lower limbs. Moreover, several identifiability conditions, which provide insights into the uniqueness (or lack thereof) and the sensitivities, are quantified and discussed. Furthermore, all the codes used in this study are openly provided, to allow other researchers to further investigate the indentation problem according to their specifications. For example, the geometries, dimensions, mesh, material models, contact parameters, and objective function formulations, can be modified. Additionally, the codes can be further modified to examine identifiability with respect to experimental data obtained by other measurement modalities, such as ultrasound or MRI.

2. Material and Methods

The codes used to conduct the simulations and analyses described in this study are freely and openly available, and can be obtained at https://github.com/SolavLab/indentify. This paper refers to release version v1.0.0.

2.1 FE model

As the framework for the current study, we implemented a simple axisymmetric model of an indentation test using the FE solver FEBio version 3.7.0 [71]. We used MATLAB 9.10 R2021a (The Mathworks Inc., Natick, MA, USA) with the GIBBON open-source toolbox version 3.5.0 [72] for preprocessing and postprocessing the simulations. All the analyses were performed on a Windows 10 PC with an Intel Core i9-11900K 3.5 GHz CPU and 32GB RAM. The model features a cylindrical specimen with radius $R^{sp} = 60\text{mm}$ and height $H^{sp} = 60\text{mm}$ representing a soft tissue bulk region, and a rigid hemisphere with radius $R^{ind} = 15\text{mm}$, representing the indenter, as shown in Fig. 1. To attain axisymmetry and reduce the computation time, we modeled the entire problem using a 2° cylindrical sector and constrained the out-of-plane motion along the tangential facing surfaces, such that the displacements u in the tangential direction are $u_\theta|_{\theta=0^\circ} = u_\theta|_{\theta=2^\circ} = 0$. During the quasi-static simulations, the lateral surface was free of traction and the bottom surface remained fully fixed.

The cylindrical specimen was meshed with quadratic elements for reducing volumetric locking effects in the nearly incompressible materials. We used quadratic 20-nodes hexahedral elements everywhere except along the centerline, where quadratic 15-nodes pentahedral elements were used, as shown in Fig.1(a). To account for the inhomogeneous deformation, we implemented a nonuniform mesh, in which the mesh is denser closer to the centerline and the upper indented surface, using a power-law distribution. The mesh consists of $10N \times 5N \times 1$ elements along the radial, axial and tangential directions, respectively, where $N \in \mathbb{N}$ is the mesh-density factor. The element sizes are driven by (1.1) and (1.2), which formulate the vertices coordinates r_m and z_n in the radial and axial directions, respectively, as demonstrated in Fig.1.

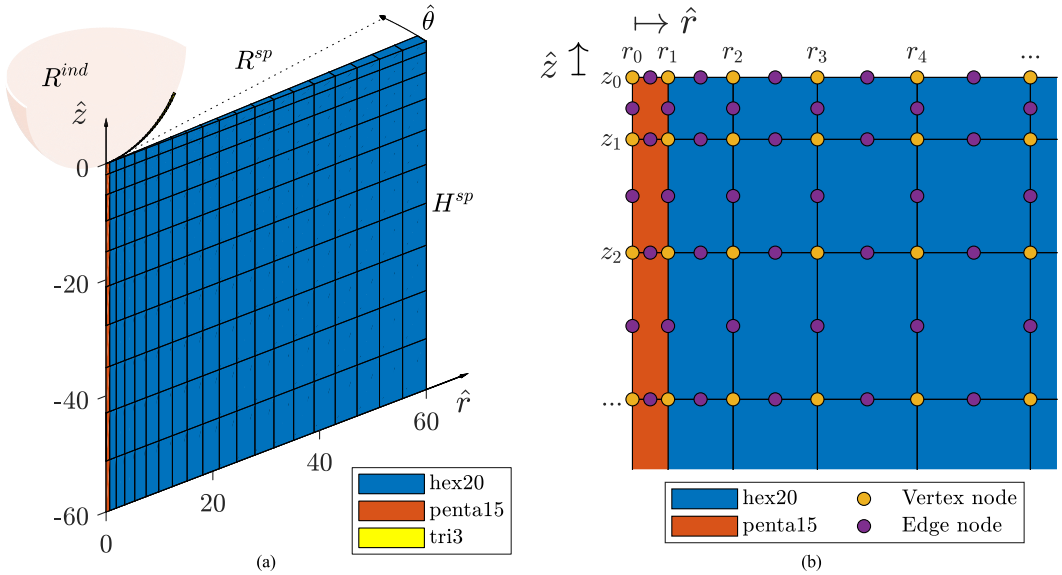

Fig. 1. The axisymmetric FE model used for all indentation analyses. A 2° cylindrical sector of the specimen and hemispherical indenter represent the axisymmetric problem. (a) a 3D view of the nonuniform mesh consisting of quadratic hexahedral (hex20) and pentahedral (penta15) elements for the specimen, and linear triangular elements (tri3) for the rigid indenter. (b) A close up view in the $\hat{r} - \hat{z}$ plane of the specimen, for visualizing the vertex nodes ordering scheme according to (1.1)-(1.2).

$$\begin{cases} r_m = \left(\frac{m}{10N}\right)^{\beta_R} R^{sp}, \qquad m = 0,1,\dots,10N & (1.1) \\ z_n = -\left(\frac{n}{5N}\right)^{\beta_H} H^{sp}, \qquad n = 0,1,\dots,5N & (1.2) \end{cases}$$

where β_R and β_H control the amount of density bias towards the centerline and upper surface, respectively. In the current study we used $\beta_R = \beta_H = 1.5$. The edge nodes of the quadratic elements were positioned at mid-edge, as shown Fig. 1(b) – depicted in purple. Based on a mesh convergence test (further discussed in the Results section) we selected a value of $N = 2$ for all simulations, which resulted in a total of 1574 nodes, as shown in Fig. 1. This is equivalent to 176102 nodes in a full cylindrical model. The surface of the hemispherical rigid indenter was modeled with 51 triangular shell elements, and was prescribed with a downward vertical displacement until a final indentation depth of 10 mm was achieved. Contact was implemented using FEBio's *sliding-elastic* contact formulation [73], with a large coefficient (*fric_coeff=1×10*^{8}) to enforce a near perfect stick condition.

2.2 Constitutive models and synthetic test data

The present study focuses on four well-established isotropic two-parameter hyperelastic formulations, which are commonly used for modeling bulk soft-tissues in general, and particularly for human limbs [13], [74], [75]. Table 1 lists the constitutive law of each model, as formulated in FEBio, and their respective material parameters. To explore the sensitivities associated with each hyperelastic model, we probed a large parameter space whose range was determined based on values reported in the literature, as listed in Table 2.

In place of experimental indentation data, we used the numerical predictions of an a priori specified baseline material parameter set, $\boldsymbol{p}^*$, to create synthetic experimental data for each constitutive model. We then used the same model to investigate the mechanical response of a wide range of trial parameter sets $\boldsymbol{p}$. We consider the response of each simulation by inquiring the indenter's reaction force and the displacement of the nodes on the upper indented surface, which represent experimental measurements that are feasible in noninvasive *in-vivo* indentation tests (e.g., using a force transducer and 3D-DIC, respectively). The nodal displacements were measured at the edge and vertex nodes (see (1.1)) which are located at $r > R^{ind}$ in the reference configuration (to exclude nodes obstructed by the indenter) along the top front edge ($\theta = 0$), as illustrated in Fig. 3(b). Both measurements were taken at 5 equally spaced indentation steps: δ=2,4,6,8, and 10 mm.

2.3 Objective function analysis

A combined objective function $F_{uf}(\boldsymbol{p}, \boldsymbol{p}^*; \delta)$, was defined to account for both measurement modalities: the indenter's reaction force (f) and the upper surface nodal displacements (u). F_{uf} quantifies the combined discrepancies between the numerical predictions associated to a trial parameter set $\boldsymbol{p}$ and the baseline parameter set $\boldsymbol{p}^*$, at a given indentation depth δ, as given in (2):

$$F_{uf}(\boldsymbol{p}, \boldsymbol{p}^*; \delta) = \eta F_f(\boldsymbol{p}, \boldsymbol{p}^*; \delta) + (1-\eta) F_u(\boldsymbol{p}, \boldsymbol{p}^*; \delta), \qquad \eta \in [0,1] \tag{2}$$

Here, $F_f(\boldsymbol{p}, \boldsymbol{p}^*; \delta)$ represents the overall normalized relative errors (residuals) in the reaction force, as given by (3.1) and $F_u(\boldsymbol{p}, \boldsymbol{p}^*; \delta)$ represents the overall normalized relative errors in the displacement field, as given by (3.2):

$$\begin{cases} F_f(\boldsymbol{p}, \boldsymbol{p}^*; \delta) = \dfrac{|f(\boldsymbol{p}; \delta) - f(\boldsymbol{p}^*; \delta)|^2}{|f(\boldsymbol{p}^*; \delta)|^2} & (3.1) \\ F_u(\boldsymbol{p}, \boldsymbol{p}^*; \delta) = \displaystyle\sum_{i=1}^{N_n} \boldsymbol{w}_{\boldsymbol{n},i} \cdot \frac{\left\|\boldsymbol{u}^{(i)}(\boldsymbol{p}; \delta) - \boldsymbol{u}^{(i)}(\boldsymbol{p}^*; \delta)\right\|^2}{\|\boldsymbol{u}^{(i)}(\boldsymbol{p}^*; \delta)\|^2} & (3.2) \end{cases}$$

where $f(\boldsymbol{p}; \delta)$ and $f(\boldsymbol{p}^*; \delta)$ are the trial and baseline indentation reaction forces in the $\hat{z}$ direction during an indentation depth δ, respectively; $\boldsymbol{u}^{(i)}(\boldsymbol{p}; \delta)$ and $\boldsymbol{u}^{(i)}(\boldsymbol{p}^*; \delta)$ are the trial and baseline displacement vectors (in the $\hat{r} - \hat{z}$ plane) of the i^{th} node from the reference configuration, during an indentation depth δ, respectively; $\boldsymbol{w_n} \in \mathbb{R}^{N_n}$ is a weighting vector for the nodal displacement magnitudes ($\|\boldsymbol{w_n}\| = 1$), and $N_n \in \mathbb{N}$ is the number of surface nodes measured in the analysis. In the present work, the nodal displacement magnitudes were weighted with an inverse proportion to their initial radial coordinates:

$$\boldsymbol{w_n} = \frac{\left(\frac{1}{r_1}, \frac{1}{r_2}, \dots, \frac{1}{r_{N_n}}\right)^T}{\left\|\left(\frac{1}{r_1}, \frac{1}{r_2}, \dots, \frac{1}{r_{N_n}}\right)^T\right\|} \tag{4}$$

where the coordinates of $r_1, \dots, r_{N_n}$ correspond to the nodes highlighted in Fig. 3(b), and include both vertex nodes as defined by (1.1), and the edge nodes which are positioned at the midpoints of the edges.

$F_{uf}(\boldsymbol{p}, \boldsymbol{p}^*; \delta)$ in (2) is specifically formulated as a convex combination, such that the value of η modulates the influence of each measurement modality. Therefore, assigning $\eta = 0$ or $\eta = 1$ is equivalent to measuring the surface displacements or the indentation forces alone, respectively.

Table 1 – List of investigated material models, their names (with the acronym used throughout the paper in parentheses), examples of soft tissue studies where the models were used, their strain energy density functions, and their investigated parameters. I_1 ($\tilde{I}_1$) and I_2 ($\tilde{I}_2$) are its first and second invariants of the (isochoric) right Cauchy-Green deformation tensor $\boldsymbol{C}$ ($\tilde{\boldsymbol{C}}$), respectively, where $\tilde{\boldsymbol{C}} = J^{-\frac{2}{3}}\boldsymbol{C}$, and λ_i^2 ($\tilde{\lambda}_i^2$) are its eigenvalues. J is the determinant of the deformation gradient tensor $\boldsymbol{F}$, and κ is the bulk-like modulus, which was selected as $\kappa = p_1 \times 10^3$, to enforce near incompressibility.

Constitutive model		Strain energy density function (FEBio formulation)	Material parameters, $\boldsymbol{p}$	
			p_1	p_2
Compressible	Unconstrained Neo-Hookean (NH) [50]	$\frac{\mu}{2}(I_1 - 3) - \mu \ln J + \frac{\lambda}{2} ln^2 J$	$E = \mu\left(\frac{3\lambda+2\mu}{\lambda+\mu}\right)$	$\nu = \frac{\lambda}{2(\lambda+\mu)}$
Nearly incompressible	Uncoupled Mooney-Rivlin (MR) [15]	$C_{10}(\tilde{I}_1 - 3) + C_{01}(\tilde{I}_2 - 3) + \frac{\kappa}{2}\ln^2 J$	C_{10}	C_{01}
$\kappa = p_1 \times 10^3$	1st-order Ogden (OG) [37], [38]	$\frac{c}{m^2}\sum_{i=1}^{3}\left(\tilde{\lambda}_i^m - 1\right) + \frac{\kappa}{2}\ln^2 J$	c	m
	"Symmetric" Ogden-Moerman (OM) [35], [76]	$\frac{c}{m^2}\sum_{i=1}^{3}\left(\tilde{\lambda}_i^m + \tilde{\lambda}_i^{-m} - 2\right) + \frac{\kappa}{2} ln^2 J$	c	m

Table 2 – Parameter sets used for the analysis. For each material model $\mathcal{P} = \mathcal{P}_1 \times \mathcal{P}_2$ denotes the discrete parameter domain used for evaluating the identifiability and sensitivity. The baseline values p* represent the "true" parameters, which were selected in the middle of the range.

Material model	Parameter domains, $\mathcal{P} = \mathcal{P}_1 \times \mathcal{P}_2$		Baseline values, $\boldsymbol{p}^*$		Total number of parameter sets
	$\mathcal{P}_1$ min: step: max	$\mathcal{P}_2$ min: step: max	p_1^*	p_2^*	
NH	5:6:113 kPa	0.24:0.014:0.49	59 kPa	0.365	361
MR	1:7:120 kPa	1:7:120 kPa	57 kPa	57 kPa	324
OG	1:1:51 kPa	1:1:37	26 kPa	19	1887
OM	1:1:51 kPa	1:1:37	26 kPa	19	1887

2.4 Sensitivity assessment

For the material models used in the present study, the parameters p_1 and p_2 neither share the same physical significance nor the same units for some. To allow for a comparative analysis between the identifiability of p_1 and p_2, we nondimensionalized the main material axes of the objective function $P = (p_1, p_2)$, by normalizing them by $\boldsymbol{p}^*$, resulting in the dimensionless parameter space denoted by $\bar{P} = (\bar{p}_1, \bar{p}_2)$, where $\bar{\boldsymbol{p}} = \left(\frac{p_1}{p_1^*}, \frac{p_2}{p_2^*}\right)$. Noting that the baseline parameter set $\boldsymbol{p}^*$ maps to $\bar{\boldsymbol{p}}^* = (1,1)$ by definition, the dimensionless form of (2) can be written as

$$\bar{F}_{fu}(\bar{\boldsymbol{p}}; \delta) = \eta \bar{F}_f(\bar{\boldsymbol{p}}; \delta) + (1 - \eta)\bar{F}_u(\bar{\boldsymbol{p}}; \delta), \ \eta \in [0,1] \tag{5}$$

Next, we quantified the sensitivity of $\bar{F}_{fu}(\bar{\boldsymbol{p}})$ with respect to each measurement modality, by computing the second order approximation in the neighborhood of the global minimum $\bar{\boldsymbol{p}}^*$:

$$\tilde{F}_{fu}(\bar{\boldsymbol{p}}; \delta) = \frac{1}{2}(\bar{\boldsymbol{p}} - \bar{\boldsymbol{p}}^*)^T \boldsymbol{H}_{\bar{\boldsymbol{p}}^*}(\bar{\boldsymbol{p}} - \bar{\boldsymbol{p}}^*), \tag{6}$$

where $\bar{\boldsymbol{H}}^* \in \mathbb{R}^{2\times 2}$ is the Hessian matrix of $\bar{F}_{fu}(\bar{\boldsymbol{p}})$ evaluated at $\bar{\boldsymbol{p}}^*$, whose elements are defined by

$$\bar{H}_{ij}^* = \left(\frac{\partial^2 \bar{F}_{fu}}{\partial \bar{p}_i \partial \bar{p}_j}\right)_{\bar{\boldsymbol{p}}=\bar{\boldsymbol{p}}^*}, \qquad 1 \le i,j \le 2 \tag{7}$$

The partial derivatives in (7) were approximated using the central finite-difference method, using the data points corresponding to the trial parameter sets that are within a 9x9 grid centered at $\bar{\boldsymbol{p}}^*$. Note that in the present study $\dim(\bar{\boldsymbol{p}}) = 2$, hence the approximation given in (6) has the shape of an ellipsoid with isolines tracing ellipses. For any value $\Delta\bar{F} > 0$, we define the parameter indifference region [54] $\Omega_{\Delta\bar{F}}$, as:

$$\Omega_{\Delta\bar{F}} \triangleq^{\text{def}} \left\{\bar{\boldsymbol{p}} \in \bar{P}:\ \tilde{F}_{fu}(\bar{\boldsymbol{p}}; \delta) \le \Delta\bar{F}\right\} \tag{8}$$

The material parameter identifiability was then locally assessed using the following Hessian-based metrics, commonly used for optimal design of experiments [54], [77], [78]:

(M1) $det(\bar{\boldsymbol{H}}^*)$ – the determinant of the Hessian is inversely proportional to the volume of the indifference region, which should be minimized to obtain optimal identifiability (*M1* should be maximized).

(M2) $cond(\bar{\boldsymbol{H}}^*)$ – the condition number of the Hessian equals the ratio of the largest to smallest eigenvalues of the Hessian (which relates to the aspect ratio of the ellipse in our case of two parameters), and therefore should be minimized towards the one for optimal identifiability of both parameters.

(M3) $det(\tilde{\boldsymbol{H}}^*)$, where $\tilde{\boldsymbol{H}}^*$ is the scaled Hessian, whose elements are defined by $\tilde{H}_{ij}^* = \bar{H}_{ij}^* / \left(\bar{H}_{ii}^* \bar{H}_{jj}^*\right)^{-1/2}$ (no summation on *i* or *j*), which indicates the interaction between the parameter estimates, or the alignment of ellipse's principal axes to material axes in our case. When this metric is maximized towards one, there is minimal interaction, which means that changes in one parameter have minimal effects on the other.

3. Results

3.1 Mesh convergence study

An FE mesh convergence study was performed by comparing the numerical predictions of the indentation force and the surface displacement field for various values of the mesh refinement factor N (see (1)), for the OG material model. A very fine mesh ($\tilde{N} = 20$) served as the "true" data for evaluating the following mesh convergence errors:

$$E_F(N) = 100\% \cdot \frac{\left|F(N) - F(\tilde{N})\right|}{\left|F(\tilde{N})\right|} \tag{9.1}$$

$$E_u(N) = 100\% \cdot \frac{1}{N_n(N)} \sum_{i=1}^{N_n(N)} \frac{\left\|\boldsymbol{u}^i(N) - \boldsymbol{u}^i(\tilde{N})\right\|}{\left\|\boldsymbol{u}^i(\tilde{N})\right\|} \tag{9.2}$$

where $F(N)$ and $F(\tilde{N})$ denote the maximal indentation forces (at $\delta = 10\ mm$) resulting from the respective mesh density factor, and $N_n(N)$ is the number of nodes used in the analysis. The vector $\boldsymbol{u}^i(N)$ denotes the i^{th} node approximated final displacement using a mesh factor N, while the vector $\boldsymbol{u}^i(\tilde{N})$ denotes the "true" final displacement of the i^{th} node, obtained by interpolating the numerical results of $\tilde{N} = 20$ (141,725 nodes and 20,522 elements) with the quadratic shape functions.

Figs. 2(a) and 2(b) present the relative errors in the indentation force $E_f(N)$ and the mean absolute percentage error in the nodal displacements $E_u(N)$, respectively, for values of N between 1-7. Fig. 2(a) also shows the simulation elapsed time as a function of the mesh refinement factor N. To account for the broad range of tested material parameters (see Table 2), we repeated the analysis using the most compliant and stiff sets $\boldsymbol{p}_{min} = \min \mathcal{P}_{OG}$ and $\boldsymbol{p}_{max} = \max \mathcal{P}_{OG}$, respectively. For both sets, a mesh refinement factor $N = 2$ yields relative indentation force errors $E_f(N)$ below 1% and $E_u(N)$ below 5.2%, while maintaining a short runtime of below 13 seconds. Furthermore, for values $N \geq 3$ the elapsed time is shown to increase sharply. Similarly, an initial steep improvement in the calculated nodal displacement error, $E_u(N)$, is noticeable between $N = 1$ and $N = 2$ (Fig. 2(b)). As a compromise between the increased accuracy and elapsed times, we chose to proceed to use $N = 2$ (1574 nodes and 251 elements) for all simulations.

3.2 Reaction forces and surface displacement results

Fig. 3 shows an example for the numerical results that were used to evaluate the objective function, using the OG material with parameters $\boldsymbol{p}^* = (26\ \text{kPa}, 19)$. Fig. 3(a) shows the indentation-force vs. indentation-depth curve from which $F_f(\boldsymbol{p}, \boldsymbol{p}^*; \delta)$ was calculated. Fig. 3(b) depicts a snapshot of the deformed specimen at $\delta = 10\ mm$, where the displacements of the highlighted nodes serve as input for $F_u(\boldsymbol{p}, \boldsymbol{p}^*; \delta)$.

3.3 Objective function visualization

For each material model we evaluated the objective function using the corresponding parameter sets $\boldsymbol{p} \in \mathcal{P}$, with respect to the baseline set $\boldsymbol{p}^*$, as given in Table 2. Figs. 4-7 visualize the objective functions for the NH, MR, OG, and OM material models, respectively. Panel (a) in each figure consist of a grid of contour plots presenting the shape of $\bar{F}_{fu}$ (5); each row represents the data collected at a certain indentation step: δ=2,4,6,8 and 10mm, and the columns represent various values of the mixing parameter η. Each consecutive contour line represents a 5% increase in the mean relative error, and is identified by a unique color. Notice that the objective function is defined in terms of squared relative errors rather than percentage error, hence the resulting colormap is nonlinear (e.g., a 5% mean squared relative error corresponds to a value of 0.05^2 in the objective function). The white contour lines and the magenta ellipses represent the isolines of the objective function $\bar{F}_{fu} = 0.1^2$, and of the quadratic approximation (6) $\tilde{F}_{fu} = 0.1^2$, respectively. As such, the area inside the magenta ellipses depicts the parameter indifference region $\Omega_{0.01}$, as defined in (8). Finally, the dashed green lines illustrate the principal axes of $\tilde{F}_{fu}$ (eigenvectors of the Hessian). Note that their displayed length is arbitrary and should not be interpreted as a magnitude of the eigenvalues.

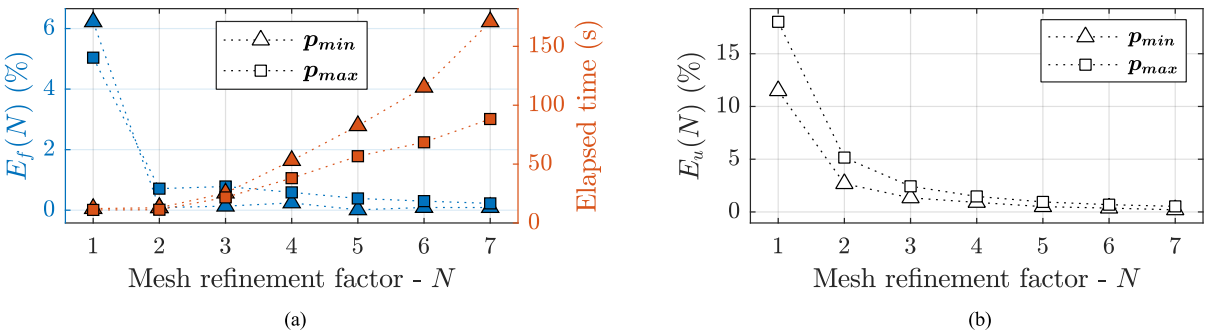

Fig. 2. Mesh convergence study results. The OG material model was used with the most compliant and stiff parameter sets $\boldsymbol{p}_{min} = (1\ \text{kPa}, 1)$ and $\boldsymbol{p}_{max} = (51\ \text{kPa}, 37)$, respectively, to produce: (a) the relative indentation force error and the simulation elapsed time, and (b) the mean absolute percentage error in the surface nodal displacements.

Figs. 4-7 panels (b), (c) and (d), feature heatmaps representing the Hessian-based metrics *M1*, *M2* and *M3*, respectively, associated with each cell in their respective panel (a). The blank squares represent invalid data due to indefinite Hessian approximations. This phenomenon was observed with objective functions shaped as long valleys, in which one of the principal curvatures is zero or positive yet negligible in magnitude. For example, the Hessian corresponding to the objective function featured in the bottom right cell in Fig. 6(a),

$$H \approx \begin{bmatrix} 0.4116 & 0.4968 \\ 0.4968 & 0.5954 \end{bmatrix} \tag{10}$$

is indefinite since its eigenvalues are $\lambda_1 \approx 1.0087$ and $\lambda_2 \approx -0.0017$. In cases of this sort, the quadratic approximation $\tilde{F}_{fu}$ in (6) describes a hyperbolic paraboloid instead of an elliptic paraboloid, thereby rendering the metrics *M1-M3* meaningless.

3.4 Identifiability from indentation force data

The right most column in Figs. 4-7 (a) represent the objective function when considering only the residuals in the indentation forces, i.e., $\bar{F}_{fu}(\bar{\boldsymbol{p}}; \delta) \equiv \bar{F}_f(\bar{\boldsymbol{p}}; \delta)$. The resulting objective function for the neo-Hookean model depicted in Fig. 4(a), has the shape of a long and narrow valley, which runs parallel to the $\bar{p}_2$ (ν) axis. This implies that the same force-depth response is generated by different sets of parameter values along the valley, making the "true" parameter unidentifiable. Moreover, the shape is unchanged by varying the indentation depth. A similar shape can also be observed for δ=2mm in the upper right cells in Figs. 6(a) and 7(a), depicting $\bar{F}_f$ for the OG and OM material models, respectively. However, in contrast to the straight valley appearing in the NH results, these valleys follow a slight curvature, which is more accentuated as δ increases. The effect of indentation depth can also be seen by the rotation of the green dashed lines representing the principal axes of the approximation. The results of the MR model in Fig. 5(a), depict a straight valley along the line $\bar{C}_{10} + \bar{C}_{01} = 2$, which remains constant throughout the indentation process. For all four material models, both the parameter indifference regions and the corresponding highlighted contours, are not fully confined within the tested range of parameters, which attribute to infinite areas (or volumes).

3.5 Identifiability from surface deformation data

The left most columns in Figs. 4-7(a) represent the objective function when only surface displacements are considered, i.e., $\bar{F}_{fu}(\bar{\boldsymbol{p}}; \delta) \equiv \bar{F}_u(\bar{\boldsymbol{p}}; \delta)$. In the case of the NH, OG, and OM material models, the objective function appears as a straight and symmetric valley, parallel to $\bar{p}_1$, as shown in the left column of Figs. 4(a), 6(a), and 7(a), respectively. The parameter indifference regions representing a 10% relative error (indicated by the magenta and white overlapping curves) span the entire tested range of $\bar{p}_1$ during all five indentation steps. For the OG material, the curvature in the vertical direction (H_{22}) increases monotonically with indentation depth up to the final indentation step. A similar trend can be seen for the OM model during only the first four steps, after which the curvature decreases. For the NH model it remains constant during the entire indentation process. In addition to the horizontal valley, the OG model exhibits a horizontal ridgeline below $\bar{p}_2 = 1$, as seen for δ=4,6mm in Fig. 6(a). Note that this feature remains present but becomes invisible at δ= 8,10mm due to exceeding the colorbar's limit.

3.6 Identifiability from indentation force and surface deformation data

Recalling the formulation of $\bar{F}_{fu}$ given in (5), assigning $0 < \eta < 1$ results in objective functions that combine the residuals in both the indentation forces and the surface displacements, which are presented in the three middle columns in Figs. 4(a)-7(a) for η=0.25, 0.5 and 0.75. The effect of combining both measurement modalities is readily apparent by the presence of

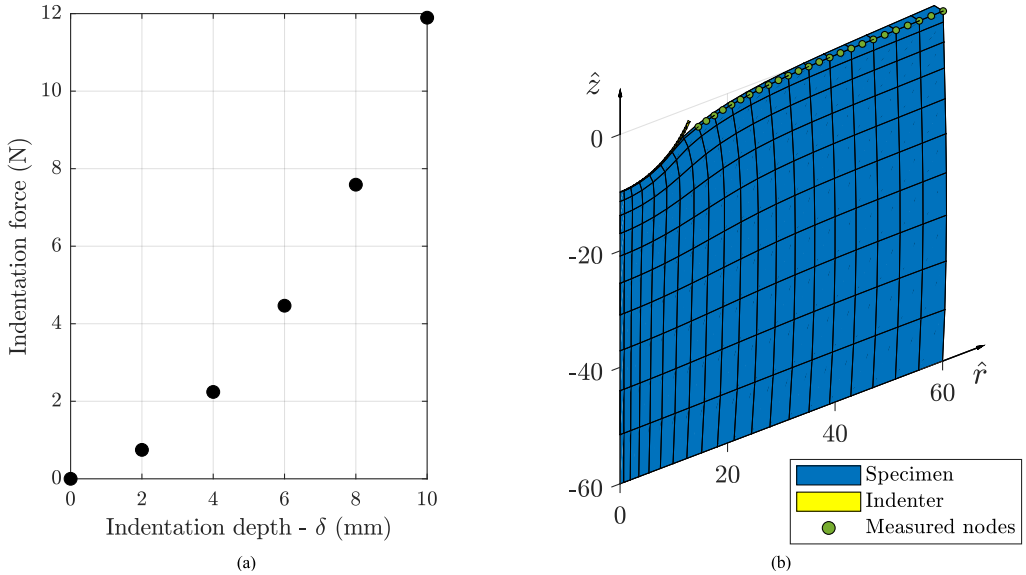

Fig. 3. Exemplary results from a simulation using OG material model with parameters $\boldsymbol{p} = (26\,\text{kPa}, 19)$. (a) The indentation-force vs. indentation-depth curve used for calculating F_f (3.1) in the objective function. (b) A snapshot of the deformed specimen at δ=10mm. The positions of the highlighted nodes are sampled at each indentation step for calculating F_u (3.2) in the objective function.

tighter indifference regions than those obtained by using either one alone. In Fig. 4(a), for example, the contour lines transition from parallel horizontal (infinite area) to oval (finite area), and finally to parallel vertical (infinite area again), as η grows from 0 to 1. An example of the effect of η on the aspect ratio of the parameter indifference region is demonstrated by the heatmap of $cond(\bar{\boldsymbol{H}}^*)$ for the NH model in Fig. 4(c). An example of the influence of indentation depth on the indifference region area is demonstrated by the heatmap of $det(\bar{\boldsymbol{H}}^*)$ for the OG model in Fig. 6(b), where the area is shown to monotonically decrease with the indentation depth.

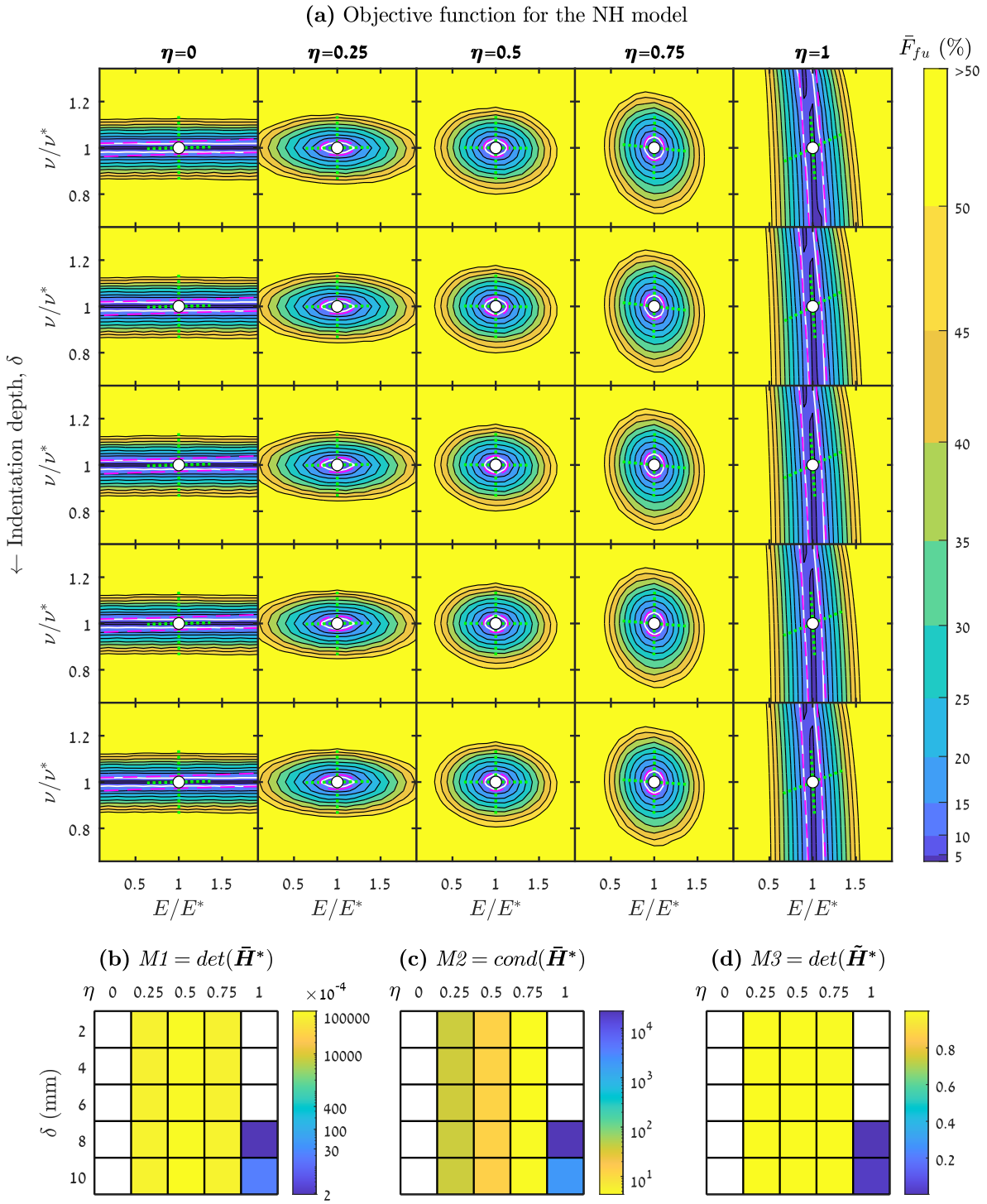

Fig. 4. Results of NH material model with $\boldsymbol{p}^* = (59\ \text{kPa}, 0.365)$. Top: (a) the contour plots depict the shape of $\bar{F}_{fu}(\bar{\boldsymbol{p}}; \delta)$ at various indentation depths δ=2,4,6,8 and 10mm, and values of η. The white and magenta curves indicate the isolines representing a 10% error, $\bar{F}_{fu}(\bar{\boldsymbol{p}}; \delta) = 0.1^2$ and $\tilde{F}_{fu}(\bar{\boldsymbol{p}}; \delta) = 0.1^2$, respectively. The dashed green lines illustrate the principal axes of $\tilde{F}_{fu}$. Bottom: Heat maps of the nondimensional Hessian-based metrics: (b) *M1*, (c) *M2*, and (d) *M3*. Blank squares indicate invalid results due to indefinite Hessian approximations. The quantities depicted in (b) and (c) are presented by a logarithmic color scale, and the colorbar in (b) is intentionally flipped since *M2* should be minimized while *M1* and *M3* should be maximized.

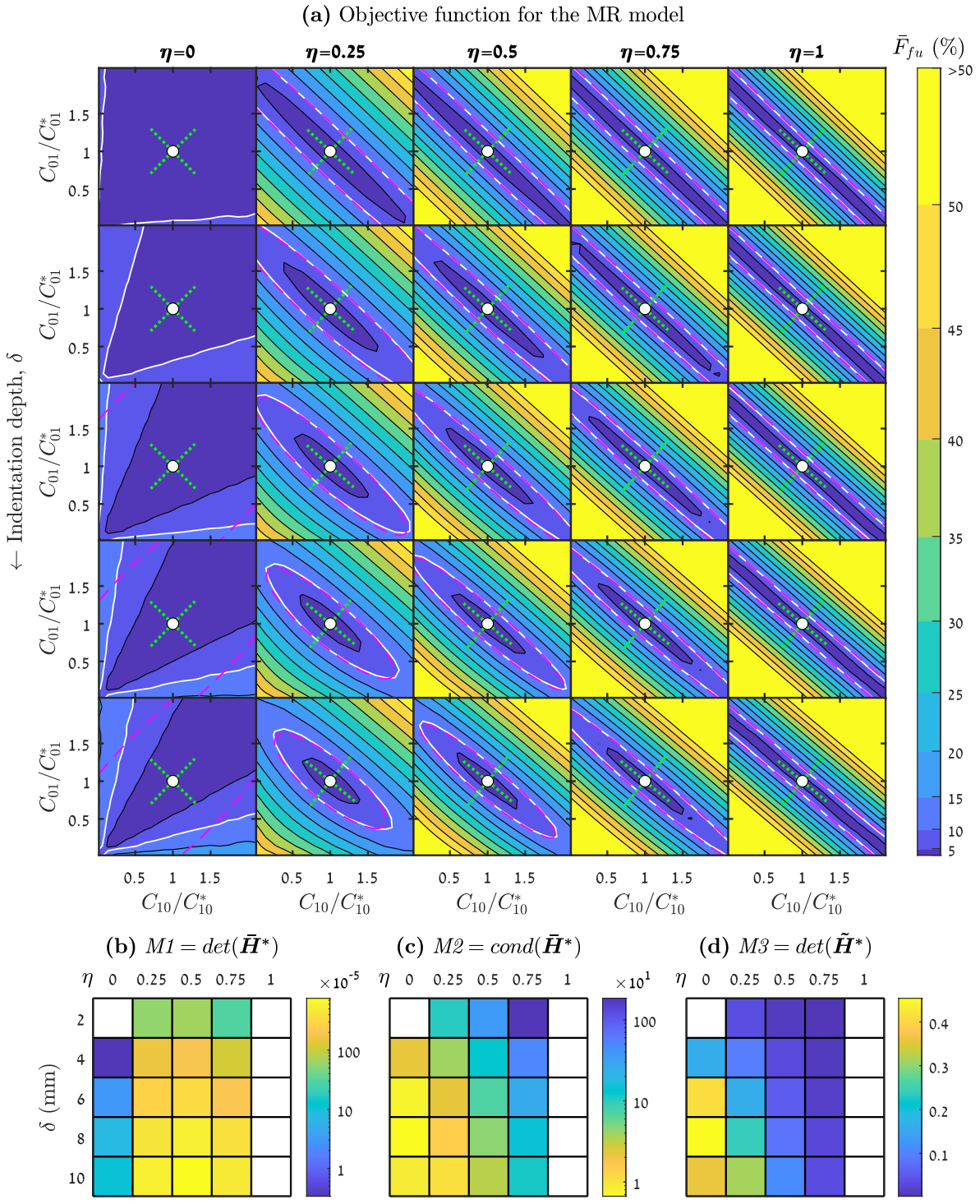

Fig. 5. Results of MR material model with $\boldsymbol{p}^* = (57\ kPa, 57\ kPa)$. Top: (a) the contour plots depict the shape of $\bar{F}_{fu}(\bar{\boldsymbol{p}}; \delta)$ at various indentation depths δ=2,4,6,8 and 10mm, and values of η. The white and magenta curves indicate the isolines representing a 10% error, $\bar{F}_{fu}(\bar{\boldsymbol{p}}; \delta) = 0.1^2$ and $\tilde{F}_{fu}(\bar{\boldsymbol{p}}; \delta) = 0.1^2$, respectively. The dashed green lines illustrate the principal axes of $\tilde{F}_{fu}$. Bottom: Heat maps of the nondimensional Hessian-based metrics: (b) *M1*, (c) *M2*, and (d) *M3*. Blank squares indicate invalid results due to indefinite Hessian approximations. The quantities depicted in (b) and (c) are presented by a logarithmic color scale, and the colorbar in (b) is intentionally flipped since *M2* should be minimized while *M1* and *M3* should be maximized.

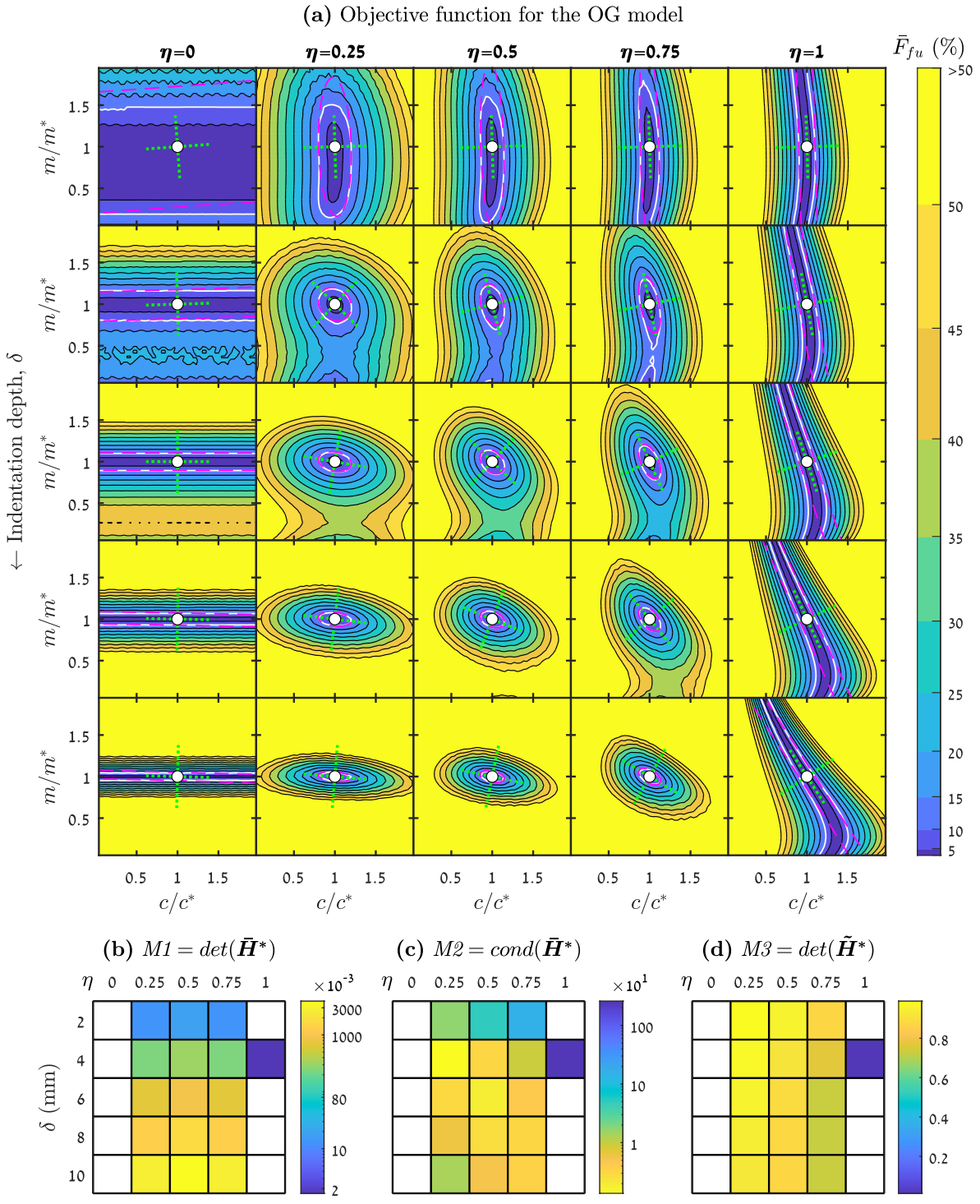

Fig. 6. Results of OG material model with $\boldsymbol{p}^* = (26\,kPa, 19)$. Top: (a) the contour plots depict the shape of $\bar{F}_{fu}(\bar{\boldsymbol{p}}; \delta)$ at various indentation depths δ=2,4,6,8 and 10mm, and values of η. The white and magenta curves indicate the isolines representing a 10% error, $\bar{F}_{fu}(\bar{\boldsymbol{p}}; \delta) = 0.1^2$ and $\tilde{F}_{fu}(\bar{\boldsymbol{p}}; \delta) = 0.1^2$, respectively. The dashed green lines illustrate the principal axes of $\tilde{F}_{fu}$. Bottom: Heat maps of the nondimensional Hessian-based metrics: (b) *M1*, (c) *M2*, and (d) *M3*. Blank squares indicate invalid results due to indefinite Hessian approximations. The quantities depicted in (b) and (c) are presented by a logarithmic color scale, and the colorbar in (b) is intentionally flipped since *M2* should be minimized while *M1* and *M3* should be maximized.

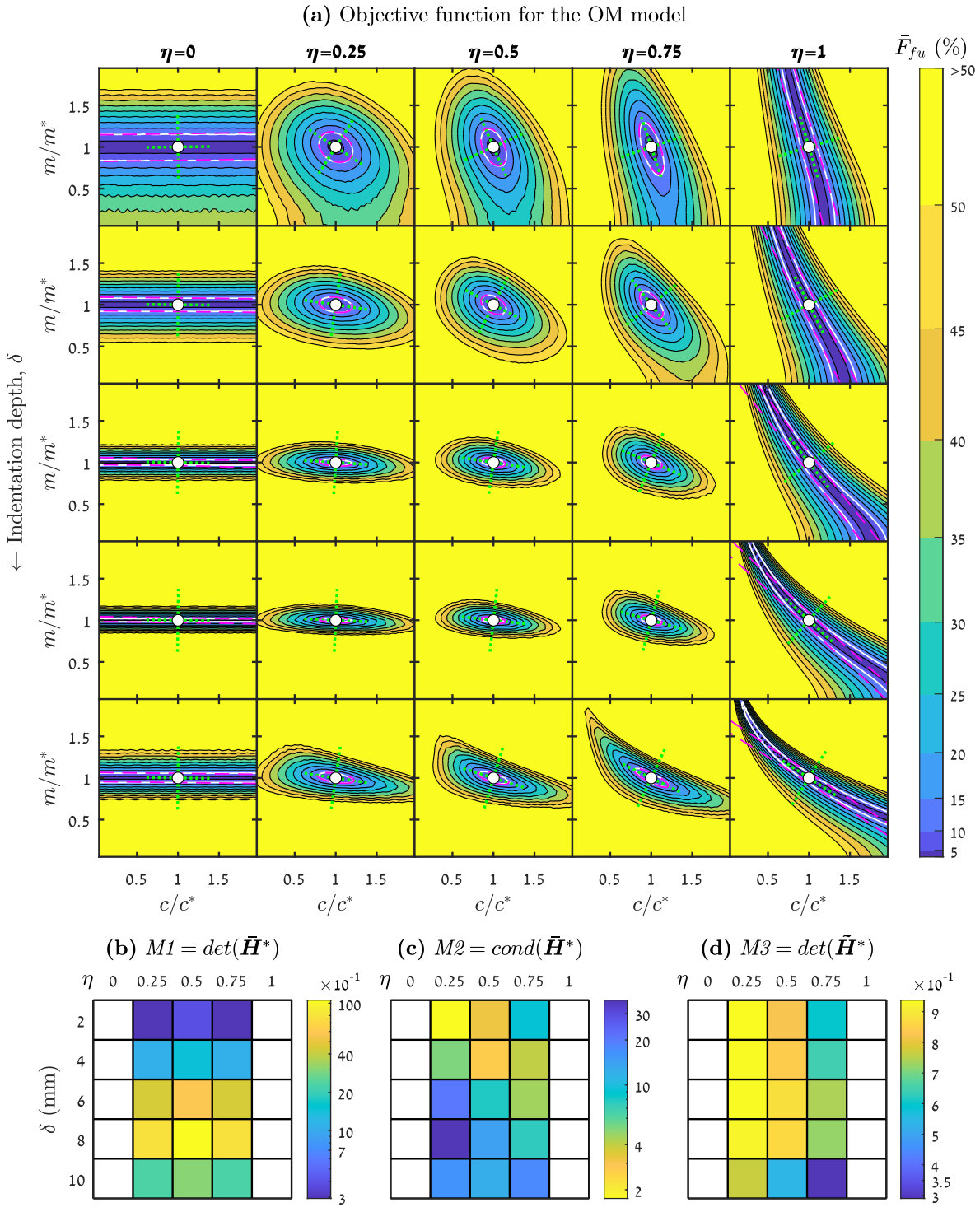

Fig. 7. Results of OM material model with $\boldsymbol{p}^* = (26\ \text{kPa}, 19)$. Top: (a) the contour plots depict the shape of $\bar{F}_{fu}(\bar{\boldsymbol{p}}; \delta)$ at various indentation depths δ=2,4,6,8 and 10mm, and values of η. The white and magenta curves indicate the isolines representing a 10% error, $\bar{F}_{fu}(\bar{\boldsymbol{p}}; \delta) = 0.1^2$ and $\tilde{F}_{fu}(\bar{\boldsymbol{p}}; \delta) = 0.1^2$, respectively. The dashed green lines illustrate the principal axes of $\tilde{F}_{fu}$. Bottom: Heat maps of the nondimensional Hessian-based metrics: (b) *M1*, (c) *M2*, and (d) *M3*. Blank squares indicate invalid results due to indefinite Hessian approximations. The quantities depicted in (b) and (c) are presented by a logarithmic color scale, and the colorbar in (b) is intentionally flipped since *M2* should be minimized while *M1* and *M3* should be maximized.

4. Discussion

This study investigated the material parameter identifiability from simulated indentation tests data for several hyperelastic constitutive models with two parameters each. These material models and test type are especially relevant to applications where soft tissues are required to be characterized *in-vivo*, and specimens cannot be excised for performing other standard mechanical tests. We used constitutive models and parameter values from the literature, representing human limb bulk soft tissue regions. However, the proposed framework can be easily adapted to other models and parameter values. We used an idealized identification problem, free of model-fidelity and measurement errors, as further discussed in sub-section 4.5. The framework was devised in such way, as to gain perspectives on the utility of each measurement modality in identifying the parameters of the four hyperelastic laws.

The agreements between the isolines of the objective function and its respective approximation is apparent in every contour plot, with the exception of the left most column in Fig. 6(a), for which the values (and gradients) of the objective function in the selected range were considerably smaller than in all other cases. This suggests that the quadratic approximation performs well, even at a 10% relative error. Furthermore, we quantified the identifiability based on numerical metrics, which may be used to generalize this approach for evaluating the identifiability of parameter sets with more than two parameters, for which the contour plot visualizations become impractical.

Our results showed that when only the force-depth response was used to construct the objective function, none of the constitutive models were fully identifiable when considering individual indentation depths, i.e., the same response could be generated by different sets of parameter values. We further demonstrated that the identifiability of parameters was improved when surface displacement field data was added to the objective function. As such, when using only force-depth data as the objective function (as commonly done in the past), initializing the optimization routine from a difference set of parameters will result in convergence to a minimum that does not necessarily represents the correct parameter set. To this end, identification efforts often involve multiple starting points optimization [59], [79]. However, a systematic procedure for selecting these points remains unstandardized. An alternative method involves using genetic or evolutionary algorithms that are globally convergent [80]. Another critical factor known to limit the accuracy of the identified parameters is the ability to resolve a unique set of parameters due to lack of sensitivity of the objective function, i.e., a small curvature around the converged set. Even if the global minimizer of the objective function is identified, uncertainties in the objective function induced by the experimental data (e.g., measurement errors and inaccurate boundary conditions), must be considered. Consequently, the indifference region about the converged point should be minimized to increase the accuracy of identification. In other words, the objective function must be as sensitive as possible to perturbations from the "true" parameters. The analysis presented in this paper provides *a priori* insights into the outcomes of such experimental studies. The following sub-sections discuss each of the investigated constitutive models.

4.1 Compressible Neo-Hookean (NH)

The results of the NH model indicate that $\bar{F}_f$ is sensitive only to E while F_u is insensitive only to ν. This suggests that both indentation forces and surface measurements are necessary to identify a unique global minimum. This is made visible by the closed elliptical shapes of the combined objective function $\bar{F}_{uf}$ in Fig. 4(a), which varies with the value of η. Interestingly, this result resembles that of uniaxial tension, where E is obtained from the force-displacement (or the uniaxial stress-strain) curve and ν can be obtained by imaging the lateral strain, despite the stark difference between the deformation modes of these two tests. It should be noted that for this material model, both $\bar{F}_f$ and $\bar{F}_u$ do not vary as the indentation depth increases. Nonetheless, multiple indentation steps might still be valuable whether for reducing the signal-to-noise ratio, collecting a richer statistical data set, or for refuting the appropriateness of the NH model in the numerical model.

4.2 Nearly-incompressible Mooney-Rivlin (MR)

The results of the MR model indicate that $\bar{F}_f$ is sensitive only with respect to $C_{10} + C_{01}$, which equals half of the initial shear modulus for this material model; thereby implying that measurements of the indentation forces alone are insufficient to identify a unique set of parameters. The problem of nonuniqueness in the identified parameters for the MR material model was previously addressed in [11], which provided a comparison between the parameters identified from a uniaxial tensile test and those obtained from an indentation using indentation-force driven iFEA. The authors identified that multiple parameter sets exist along a valley of possible solutions, hence explaining the large identification errors reported: 12.5% and -103% for C_{10} and C_{01}, respectively. Using the data reported in [11], we see that despite the large estimation error of each parameter individually, the quantity $C_{10} + C_{01}$ is estimated with only -6.7% error. Another interesting observation is the shape of $\bar{F}_f$ which remained unchanged during the various indentation steps, much like in the NH model. This implies that the contribution of multiple indentation depths to parameter identification is only in providing a richer statistical data set or refuting the appropriateness of the MR model in the numerical model, but not in reducing the indifference region in the idealized analysis.

We have found that the surface displacement residuals provide poor identifiability, as $\bar{F}_u$ shows low sensitivity to either parameter, as seen in Fig. 5(a). Although some sensitivity with respect to C_{10}/C_{01} begins to show during the larger indentation depths, its subtleness will most likely deem it irrelevant for practical applications, where modeling and measurements errors may prevail. Interestingly, the symmetry of $\bar{F}_u$ along $\bar{C}_{10} = \bar{C}_{01}$ was captured well in the calculation of the Hessian, which resulted in a quadratic approximation $\tilde{F}_u$ whose major axes are perpendicular to that of $\tilde{F}_f$. Consequently, the complementary

sensitivities of these two measurement modalities are reflected by the closed ellipses shown in Fig. 5(a) representing $\bar{F}_{uf}$ ($0 < \eta < 1$). However, the ability to reliably identify a unique set of parameters remains limited.

4.3 First-order Ogden (OG) and Ogden-Moerman (OM)

The results for both OG and OM material models suggest that indentation forces alone do not provide the sufficient sensitivity needed to identify a unique set of material parameters when considering individual indentation depths, as indicated by the indifference regions of $\bar{F}_f$, which span the entirety of $\mathcal{P}_2$ (see Table 2). At lower indentation depths (e.g., $\delta = 2mm$) the contour lines of $\bar{F}_f$ are nearly parallel to the m axis, indicating that it is highly sensitive to c and indifferent to m. This implies that c could be identified by solving a simple single-variable optimization problem, regardless of the initial guess of m. The strong sensitivity with respect to c is to be expected, as the initial shear moduli of the OG and OM models are given by $\mu = c/2$ and $\mu = c$, respectively. If the strains are sufficiently small, then the Hertzian contact theory predicts a linear relation between the indentation force and the Young's modulus [47], which itself proportional to the shear modulus in an incompressible solid. Moreover, at sufficiently small indentation depths the value of m does not play a significant role due to the small deformations induced in the specimen (values of $\tilde{\lambda}_i$ are close to one), thereby explaining the insensitivity to m. At larger indentation depths, large identification errors may occur for both parameters of either material model, due to the formation of a bend in the valley, which is no longer as parallel to the m axis. It should be noted that the increase of bending in the valley at larger indentation depths could be utilized for gaining added identifiability by considering the multiple indentation depths simultaneously. For example, the uncertainty of m in both OG and OM models could be improved by considering the average of $\bar{F}_f(\bar{\boldsymbol{p}}; \delta)$ given by

$$\bar{F}_f^{tot}(\bar{\boldsymbol{p}}) = \frac{1}{N_t}\sum_{k=1}^{N_t} \bar{F}_f(\bar{\boldsymbol{p}}; \delta_k) \tag{11}$$

where $N_t = 5$, as illustrated in Fig. 8(a) and Fig. 8(b) respectively. Notice that the quadratic approximation of the averaged function is equal to the average of the quadratic approximation due to linearity. The effect of combining multi-step data is clearly made visible by observing the parameter indifference regions $\Omega_{0.1^2}$ (magenta ellipses), which no longer span the entirety range of $\bar{m}$, as seen in Fig. 6(a) and Fig. 7(a). However, despite constituting a substantial improvement over using a single indentation step, the results shown in Fig. 8(a) suggest that indentation forces alone remain unsatisfactory for accurately identifying the parameters, which is evident by the parameter indifference region $\bar{F}_f^{tot}(\bar{\boldsymbol{p}}) \leq 0.1^2$, which spans approximately $\pm 50\%$ of m^* (Fig 8a). This implies that a 10% measurement error would translate to a $\sim 100\%$ uncertainty in the estimation of m. The difficulty of identifying a unique set of OG parameters from multiple indentation force-depth datapoints was previously addressed in [11], supporting our findings despite multiple differences between the models.

Like the force measurements alone, the results show that surface displacement measurements alone cannot be used to identify a unique set of parameters. In stark contrast to $\bar{F}_f$ however, the surface displacement objective function $\bar{F}_u$ is completely insensitive to c at every indentation step for both materials. This is to be expected since these data lack any information on the applied load. Furthermore, $\bar{F}_u$ is highly sensitive to m during the deeper indentations of both materials, yet a lack of sensitivity at shallower depths is prominent (especially for the OG model). This lack of sensitivity during the initial indentation steps can be explained by the same reasoning above for $\bar{F}_f$. These results indicate that full-field surface displacement measurements (especially those taken at large indentation depths) could be used to accurately identify m even without prior knowledge of c. In practice, this approach may be limited by the maximal indentation depth achievable in the experiment. Moreover, the presence of the horizontal ridgelines in the smaller values of m in the OG model should be accounted for in the optimization process. For example, when implementing a gradient descent algorithm, it may be preferable to overestimate the initial value of m or to increase the initial guess should the lower boundary constraint be met.

Simultaneously factoring both measurement modalities into the objective function, i.e., $0 < \eta < 1$, resulted in oval parameter indifference regions, which were well-fitted by tighter and rounder ellipses. These results indicate that a unique parameter set could be identified, e.g., by using a multivariable gradient descent method from any initial guess. We have also shown how the value of η affects the aspect ratio, which in turn can be used to accelerate the convergence rate.

4.4 Sensitivity analysis and visualization

The objective function visualizations in Figs. 4-7(a) provided important insight on how the identifiability of the various material parameters changes with the indentation depth and measurement modality. We have also demonstrated how these observations can be used to choose a proper optimization scheme. The quadratic approximations of the objective functions successfully captured the shape of the objective function in the proximity of the global minimum, which seemingly suggests that the numerical derivation of the Hessian produced reliable results. However, we have demonstrated that objective functions which are insufficiently convex in all directions are very likely to yield an indefinite Hessian (e.g., (10)), thereby rendering the Hessian based metrics *M1-M3* meaningless. This phenomenon may occur even when an excellent agreement between the isolines of $\bar{F}_{uf}$ and $\tilde{F}_{uf}$ is observed. Therefore, nearly singular Hessians should be dealt by with special care. An alternative formulation for criterion *M3* could be the angles between the non-degenerate eigenvectors of the Hessian and the material axes, which relate to the parameter interaction. For example, in the 2D case, the angle to the p_1 axis is given by

$$\frac{1}{2}\text{atan}\left(\frac{\bar{H}_{12}^*}{\bar{H}_{11}^* - \bar{H}_{22}^*}\right) \tag{12}$$

Due to its generality, this approach is advantageous over that defined by *M3* (section 2.6), which is undefined when $\bar{H}_{11}^{*}\bar{H}_{22}^{*} \leq 0$. In all other cases, i.e., objective functions with strictly positive Hessians, the parameter indifference region area, aspect ratio and axes alignment were successfully reflected in the heatmaps of the appropriate Hessian metrics. Although these heatmaps may seem redundant in the context of the current study, where the objective function surface could be plotted over a 2D plane, their effectiveness in identifiability studies with include a larger number of parameters is promising.

4.5 Limitations and future studies

This study entails several limitations. First, we used synthetic test data, representing an idealized identification problem where model-fidelity errors (e.g., using an inappropriate constitutive law or inaccurately modelling boundary conditions) and measurement errors (e.g., from the load cell or the camera system), are absent. In essence, our analysis assumed that there exists a *trial* parameter set for which the numerical predictions coincide with the test data, such that the objective function approaches zero. Under realistic setting this is not the case; at each indentation step the residuals of force and displacement might be minimized by a different parameter set, i.e., the global minimum of the multi-step objective function

$$F_{uf}^{tot}(\boldsymbol{p},\boldsymbol{p}^{*}) = \eta F_{f}^{tot}(\boldsymbol{p},\boldsymbol{p}^{*}) + (1-\eta)F_{u}^{tot}t(\boldsymbol{p},\boldsymbol{p}^{*}), \qquad \eta \in [0,1] \tag{13}$$

may be nonzero, where

$$\begin{cases} F_{f}^{tot}(\boldsymbol{p},\boldsymbol{p}^{*}) = \sum_{k=1}^{N_t} \boldsymbol{w}_{\boldsymbol{f}_k}\bar{F}_{f}(\bar{\boldsymbol{p}};\delta_k) & (14.1) \\ F_{u}^{tot}(\boldsymbol{p},\boldsymbol{p}^{*}) = \sum_{k=1}^{N_t} \boldsymbol{w}_{\boldsymbol{u}_k}\bar{F}_{u}(\bar{\boldsymbol{p}};\delta_k) & (14.2) \end{cases}$$

and $\boldsymbol{w_f}, \boldsymbol{w_u} \in \mathbb{R}^{N_t}$ are indentation step weighting vectors for $\bar{F}_f(\bar{\boldsymbol{p}};\delta)$ and $\bar{F}_u(\bar{\boldsymbol{p}};\delta)$, respectively. In addition, the identified parameters would depend on the selection of weighting vectors $\boldsymbol{w_n}, \boldsymbol{w_f}, \boldsymbol{w_u}$, which our analysis disregarded.

Another limitation stems for the fact that we modeled the soft tissue using only two-parameter hyperelastic materials models. This is a gross simplification of the real mechanical behavior of soft tissues, which exhibit various degrees of heterogeneity, anisotropy, viscoelasticity, and poroelasticity. These added complexities amount to a large number of parameters that need to be identified. Despite being a very cost intensive task, which might yield unreliable results, not much work has gone into investigating the identifiability problem in indentation tests. This study presents a first step in a systematic investigation aimed to determine the contribution of each measurement modality to parameter indefinability. Future studies are planned to extend the present study to more complex material models, i.e., larger parameter space and complex deformations. An interesting extension, for example, would be to investigate how ultrasound measurements could improve the identification in multi-layered indentation tests.

For numerical simplicity and efficiency, we chose to carry our analysis on an axisymmetric problem. This inherent symmetry along the nearly-incompressibility constraint may have restricted the deformation modes of the specimen and as such the identifiability of the parameters. Future work may investigate whether applying asymmetric indentation could produce richer deformations, which may enhance the identifiability if coupled with appropriate measurements. Finally, we plan to validate the findings of this paper against experimental data, by carrying out actual indentation tests on specimens for which standard mechanical tests can be performed.

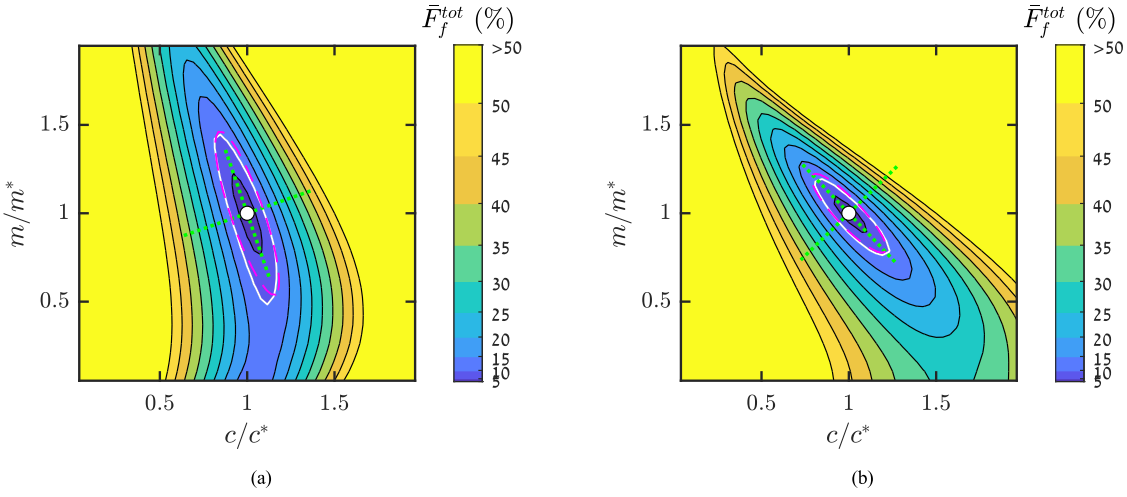

Fig. 8. Contour plots depicting the resulting shape of the objective function $\bar{F}_f^{tot}(\bar{\boldsymbol{p}})$ as given in (11), representing the average relative indentation force error during the entire indentation process, for the (a) OG and (b) OM material models. The white and magenta curves indicate the isolines representing a 10% mean relative error, $\bar{F}_f^{tot}(\bar{\boldsymbol{p}}) = 0.1^2$ and its quadratic approximation $\tilde{F}_f^{tot}(\bar{\boldsymbol{p}}) = 0.1^2$, respectively, and the dashed green lines illustrate the principal axes of $\tilde{F}_{fu}$.

5. Conclusions

This study investigated the identifiability of hyperelastic material parameters characterizing soft tissues from finite macro-indentation tests. We simulated the indentation response and quantified the discrepancies between simulated results and "true" synthetic data, to evaluate the objective functions obtained by considering the indenter's force-depth data (which is usually the only measurement used for identification) and the full-field surface displacement data (which may be measured using 3D-DIC). Our results indicated that the force-depth data was insufficient for identifying both parameters for all the constitutive laws. The addition of surface displacement data improved the parameter identifiability in all cases, but remained insufficient for the Mooney-Rivlin model. Additionally, we quantified the curvatures of the objective function using Hessian-based criteria, which can be used to generalize this approach to models with more parameters. This study provides a systematic approach for exploring parameter identifiability, and we openly provide the codes used for the simulations and analyses, making it easily translatable to many other studies. Future work could extend this framework to investigate more complex material models and measurement modalities. In conclusion, it is recommended to conduct this simulated identifiability analysis prior to any experimental data-fitting study to ensure that convergence to a unique parameter set is feasible, and to inform the experimental design.

Declaration of competing interest

The authors declare that they have no known competing financial interests or personal relationships that could have appeared to influence the work reported in this paper.

Funding

The study was supported by the Israel Science Foundation grant no. 1750/22. Dana Solav has been supported by the Jacques Lewiner Career Advancement Chair. The funders had no role in study design, data collection and analysis, decision to publish, or preparation of the manuscript.

CRediT authorship contribution statement

Zohar Oddes: Conceptualization, Methodology, Software, Formal analysis, Investigation, Visualization, Writing - Original Draft Preparation. **Dana Solav**: Conceptualization, Methodology, Software, Writing - Review & Editing, Resources, Supervision, Project administration.

References

[1] R. W. Ogden, "Nonlinear Elasticity, Anisotropy, Material Stability and Residual Stresses in Soft Tissue," in *Biomechanics of Soft Tissue in Cardiovascular Systems*, Springer Vienna, 2003, pp. 65–108.

[2] M. Chabanas, V. Luboz, and Y. Payan, "Patient specific finite element model of the face soft tissues for computer-assisted maxillofacial surgery," *Medical Image Analysis*, vol. 7, no. 2, pp. 131–151, Jun. 2003, doi: 10.1016/S1361-8415(02)00108-1.

[3] N. Cobetto, C. E. Aubin, and S. Parent, "Surgical Planning and Follow-up of Anterior Vertebral Body Growth Modulation in Pediatric Idiopathic Scoliosis Using a Patient-Specific Finite Element Model Integrating Growth Modulation," *Spine Deformity*, vol. 6, no. 4, pp. 344–350, Jul. 2018, doi: 10.1016/j.jspd.2017.11.006.

[4] A. P. del Palomar, B. Calvo, J. Herrero, J. López, and M. Doblaré, "A finite element model to accurately predict real deformations of the breast," *Medical Engineering & Physics*, vol. 30, no. 9, pp. 1089–1097, Nov. 2008, doi: 10.1016/j.medengphy.2008.01.005.

[5] Y. Payan, "Soft Tissue Finite Element Modeling and Calibration of the Material Properties in the Context of Computer-Assisted Medical Interventions," in *Material Parameter Identification and Inverse Problems in Soft Tissue Biomechanics*, S. Avril and S. Evans, Eds. Cham: Springer International Publishing, 2017, pp. 133–144. doi: 10.1007/978-3-319-45071-1_6.

[6] K. Sangpradit, H. Liu, P. Dasgupta, K. Althoefer, and L. D. Seneviratne, "Finite-Element Modeling of Soft Tissue Rolling Indentation," *IEEE Transactions on Biomedical Engineering*, vol. 58, no. 12, pp. 3319–3327, Dec. 2011, doi: 10.1109/TBME.2011.2106783.

[7] B. K. Tay, J. Kim, and M. A. Srinivasan, "In Vivo Mechanical Behavior of Intra-abdominal Organs," *IEEE Transactions on Biomedical Engineering*, vol. 53, no. 11, pp. 2129–2138, Nov. 2006, doi: 10.1109/TBME.2006.879474.

[8] F. Eggermont *et al.*, "Can patient-specific finite element models better predict fractures in metastatic bone disease than experienced clinicians?," *Bone and Joint Research*, vol. 7, no. 6, pp. 430–439, Jun. 2018.

[9] M. Hollenstein, M. Bajka, B. Röhrnbauer, S. Badir, and E. Mazza, "Measuring the In Vivo Behavior of Soft Tissue and Organs Using the Aspiration Device," in *Studies in Mechanobiology, Tissue Engineering and Biomaterials*, vol. 11, Springer, 2012, pp. 201–228. doi: 10.1007/8415_2012_120.

[10] B. Mueller, J. Elrod, O. Distler, C. Schiestl, and E. Mazza, "On the Reliability of Suction Measurements for Skin Characterization," *Journal of Biomechanical Engineering*, vol. 143, no. 2, Aug. 2021, doi: 10.1115/1.4047661.

[11] B. Pierrat, D. B. MacManus, J. G. Murphy, and M. D. Gilchrist, "Indentation of heterogeneous soft tissue: Local constitutive parameter mapping using an inverse method and an automated rig," *Journal of the Mechanical Behavior of Biomedical Materials*, vol. 78, pp. 515–528, Feb. 2018, doi: 10.1016/J.JMBBM.2017.03.033.

[12] A. Sadeghi-Naini, R. V. Patel, and A. Samani, “Measurement of Lung Hyperelastic Properties Using Inverse Finite Element Approach,” *IEEE Transactions on Biomedical Engineering*, vol. 58, no. 10, pp. 2852–2859, Oct. 2011, doi: 10.1109/TBME.2011.2160637.
[13] A. S. Dickinson, J. W. Steer, and P. R. Worsley, “Finite element analysis of the amputated lower limb: A systematic review and recommendations,” *Medical Engineering and Physics*, vol. 43, pp. 1–18, 2017, doi: 10.1016/j.medengphy.2017.02.008.
[14] D. Lacroix and J. F. Ramírez Patiño, “Finite element analysis of donning procedure of a prosthetic transfemoral socket,” *Annals of Biomedical Engineering*, vol. 39, no. 12, pp. 2972–2983, 2011, doi: 10.1007/s10439-011-0389-z.
[15] S. Portnoy, I. Siev-Ner, N. Shabshin, and A. Gefen, “Effects of sitting postures on risks for deep tissue injury in the residuum of a transtibial prosthetic-user: a biomechanical case study.,” *Computer methods in biomechanics and biomedical engineering*, vol. 14, no. 11, pp. 1009–19, 2011, doi: 10.1080/10255842.2010.504719.
[16] S. Syngellakis and M. A. Arnold, “Modelling considerations in finite element analyses of ankle foot orthoses,” in *Design and Nature VI: Comparting Design in Nature with Science and Engineering*, 2012, pp. 183–194. doi: 10.2495/DN120171.
[17] R. Pea, J. Dansereau, C. Caouette, N. Cobetto, and C.-éric É. Aubin, “Computer-assisted design and finite element simulation of braces for the treatment of adolescent idiopathic scoliosis using a coronal plane radiograph and surface topography,” *Clinical Biomechanics*, vol. 54, no. March, pp. 86–91, 2018, doi: 10.1016/j.clinbiomech.2018.03.005.
[18] J. Cheung, M. Zhang, A. Leung, and Y. Fan, “Three-dimensional finite element analysis of the foot during standing—a material sensitivity study,” *Journal of Biomechanics*, vol. 38, no. 5, pp. 1045–1054, 2005, doi: 10.1016/j.jbiomech.2004.05.035.
[19] D. Lemmon, T. Y. Shiang, A. Hashmi, J. S. Ulbrecht, and P. R. Cavanagh, “The effect of insoles in therapeutic footwear - A finite element approach,” *Journal of Biomechanics*, vol. 30, no. 6, pp. 615–620, Jun. 1997, doi: 10.1016/S0021-9290(97)00006-7.
[20] J. S. Affagard, P. Feissel, and S. F. Bensamoun, “Identification of hyperelastic properties of passive thigh muscle under compression with an inverse method from a displacement field measurement,” *Journal of Biomechanics*, vol. 48, no. 15, pp. 4081–4086, Nov. 2015, doi: 10.1016/j.jbiomech.2015.10.007.
[21] S. Avril, L. Bouten, L. Dubuis, S. Drapier, and J. F. Pouget, “Mixed experimental and numerical approach for characterizing the biomechanical response of the human leg under elastic compression,” *Journal of Biomechanical Engineering*, vol. 132, no. 3, Mar. 2010, doi: 10.1115/1.4000967.
[22] J. C. Cagle *et al.*, “A finite element model to assess transtibial prosthetic sockets with elastomeric liners,” *Medical & biological engineering & computing*, vol. 56, no. 7, pp. 1227–1240, Jul. 2018, doi: 10.1007/s11517-017-1758-z.
[23] J. W. Steer, P. A. Grudniewski, M. Browne, P. R. Worsley, A. J. Sobey, and A. S. Dickinson, “Predictive prosthetic socket design: part 2—generating person-specific candidate designs using multi-objective genetic algorithms,” *Biomechanics and Modeling in Mechanobiology*, vol. 19, no. 4, pp. 1347–1360, Aug. 2020, doi: 10.1007/s10237-019-01258-7.
[24] K. M. Moerman, D. Solav, D. M. Sengeh, and H. M. Herr, “Automated and Data-driven Computational Design of Patient-Specific Biomechanical Interfaces,” *engRxiv*, 2016, doi: 10.17605/OSF.IO/G8H9N.
[25] R. W. Ogden, G. Saccomandi, and I. Sgura, “Fitting hyperelastic models to experimental data,” *Computational Mechanics*, vol. 34, no. 6, pp. 484–502, 2004, doi: 10.1007/s00466-004-0593-y.
[26] E. Tönük and M. B. Silver-thorn, “Nonlinear Elastic Material Property Estimation of Lower Extremity Residual Limb Tissues,” *IEEE Transactions on Neural Systems and Rehabilitation Engineering*, vol. 11, no. 1, pp. 43–53, 2003, doi: 10.1109/TNSRE.2003.810436.
[27] Y. Zheng and A. F. T. Mak, “Effective elastic properties for lower limb soft tissues from manual indentation experiment,” *IEEE Transactions on Rehabilitation Engineering*, vol. 7, no. 3, pp. 257–267, Sep. 1999, doi: 10.1109/86.788463.
[28] C. W. J. Oomens, D. L. Bader, S. Loerakker, and F. Baaijens, “Pressure Induced Deep Tissue Injury Explained,” *Annals of Biomedical Engineering*, vol. 43, no. 2, pp. 297–305, 2015, doi: 10.1007/s10439-014-1202-6.
[29] J. Weickenmeier, M. Jabareen, and E. Mazza, “Suction based mechanical characterization of superficial facial soft tissues,” *Journal of Biomechanics*, vol. 48, no. 16, pp. 4279–4286, Dec. 2015, doi: 10.1016/j.jbiomech.2015.10.039.
[30] N. Briot, G. Chagnon, N. Connesson, and Y. Payan, “In vivo measurement of breast tissues stiffness using a light aspiration device,” *Clinical Biomechanics*, vol. 99, p. 105743, Oct. 2022, doi: 10.1016/j.clinbiomech.2022.105743.
[31] K. D. R. Kappert *et al.*, “In-vivo tongue stiffness measured by aspiration: Resting vs general anesthesia,” *Journal of Biomechanics*, vol. 114, p. 110147, Jan. 2021, doi: 10.1016/j.jbiomech.2020.110147.
[32] A. Nava, E. Mazza, M. Furrer, P. Villiger, and W. H. Reinhart, “In vivo mechanical characterization of human liver,” *Medical Image Analysis*, vol. 12, no. 2, pp. 203–216, Apr. 2008, doi: 10.1016/j.media.2007.10.001.
[33] N. Fougeron, P.-Y. Rohan, D. Haering, J.-L. Rose, X. Bonnet, and H. Pillet, “Combining Freehand Ultrasound-Based Indentation and Inverse Finite Element Modeling for the Identification of Hyperelastic Material Properties of Thigh Soft Tissues,” *J Biomech Eng*, vol. 142, no. 9, Sep. 2020, doi: 10.1115/1.4046444.
[34] T. Marinopoulos, L. Zani, S. Li, and V. V. Silberschmidt, “Modelling indentation of human lower-limb soft tissue: simulation parameters and their effects,” *Continuum Mechanics and Thermodynamics*, pp. 1–17, Oct. 2020, doi: 10.1007/s00161-020-00933-w.
[35] D. M. Sengeh, K. M. Moerman, A. Petron, and H. M. Herr, “Multi-material 3-D viscoelastic model of a transtibial residuum from in-vivo indentation and MRI data,” *Journal of the Mechanical Behavior of Biomedical Materials*, vol. 59, pp. 379–392, Feb. 2016, doi: 10.1016/j.jmbbm.2016.02.020.
[36] A. Gefen, M. Megido-Ravid, M. Azariah, Y. Itzchak, and M. Arcan, “Integration of plantar soft tissue stiffness measurements in routine MRI of the diabetic foot,” *Clinical Biomechanics*, vol. 16, no. 10, pp. 921–925, Dec. 2001, doi: 10.1016/S0268-0033(01)00074-2.

[37] A. Erdemir, M. L. Viveiros, J. S. Ulbrecht, and P. R. Cavanagh, “An inverse finite-element model of heel-pad indentation,” *Journal of Biomechanics*, vol. 39, no. 7, pp. 1279–1286, Jan. 2006.
[38] S. Behforootan, P. E. Chatzistergos, N. Chockalingam, and R. Naemi, “A clinically applicable non-invasive method to quantitatively assess the visco-hyperelastic properties of human heel pad, implications for assessing the risk of mechanical trauma,” *Journal of the Mechanical Behavior of Biomedical Materials*, vol. 68, pp. 287–295, Apr. 2017.
[39] C. Y. L. Chao, Y. P. Zheng, Y. P. Huang, and G. L. Y. Cheing, “Biomechanical properties of the forefoot plantar soft tissue as measured by an optical coherence tomography-based air-jet indentation system and tissue ultrasound palpation system,” *Clinical Biomechanics*, vol. 25, no. 6, pp. 594–600, Jul. 2010, doi: 10.1016/j.clinbiomech.2010.03.008.
[40] H. V. Tran, F. Charleux, M. Rachik, A. Ehrlacher, and M. C. Ho Ba Tho, “In vivo characterization of the mechanical properties of human skin derived from MRI and indentation techniques,” *Computer Methods in Biomechanics and Biomedical Engineering*, vol. 10, no. 6, pp. 401–407, 2007, doi: 10.1080/10255840701550287.
[41] R. B. Groves, S. A. Coulman, J. C. Birchall, and S. L. Evans, “Quantifying the mechanical properties of human skin to optimise future microneedle device design,” *Computer Methods in Biomechanics and Biomedical Engineering*, vol. 15, no. 1, pp. 73–82, Jan. 2012, doi: 10.1080/10255842.2011.596481.
[42] C. Pailler-Mattei, S. Bec, and H. Zahouani, “In vivo measurements of the elastic mechanical properties of human skin by indentation tests,” *Medical Engineering and Physics*, vol. 30, no. 5, pp. 599–606, Jun. 2008, doi: 10.1016/j.medengphy.2007.06.011.
[43] F. J. Carter, T. G. Frank, P. J. Davies, D. McLean, and A. Cuschieri, “Measurements and modelling of the compliance of human and porcine organs,” *Medical Image Analysis*, vol. 5, no. 4, pp. 231–236, Dec. 2001, doi: 10.1016/S1361-8415(01)00048-2.
[44] T. P. Prevost, G. Jin, M. A. de Moya, H. B. Alam, S. Suresh, and S. Socrate, “Dynamic mechanical response of brain tissue in indentation in vivo, in situ and in vitro,” *Acta Biomaterialia*, vol. 7, no. 12, pp. 4090–4101, Dec. 2011, doi: 10.1016/j.actbio.2011.06.032.
[45] A. Gefen and S. S. Margulies, “Are in vivo and in situ brain tissues mechanically similar?,” *Journal of Biomechanics*, vol. 37, no. 9, pp. 1339–1352, Sep. 2004, doi: 10.1016/j.jbiomech.2003.12.032.
[46] K. Miller, K. Chinzei, G. Orssengo, and P. Bednarz, “Mechanical properties of brain tissue in-vivo: experiment and computer simulation,” *Journal of Biomechanics*, vol. 33, no. 11, pp. 1369–1376, Nov. 2000, doi: 10.1016/S0021-9290(00)00120-2.
[47] H. Hertz, “On the contact of elastic solids,” *Z. Reine Angew. Mathematik*, vol. 92, pp. 156–171, 1881.
[48] I. N. Sneddon, “The relation between load and penetration in the axisymmetric boussinesq problem for a punch of arbitrary profile,” *International Journal of Engineering Science*, vol. 3, no. 1, pp. 47–57, May 1965, doi: 10.1016/0020-7225(65)90019-4.
[49] W. C. Hayes, L. M. Keer, G. Herrmann, and L. F. Mockros, “A mathematical analysis for indentation tests of articular cartilage,” *Journal of Biomechanics*, vol. 5, no. 5, pp. 541–551, Sep. 1972, doi: 10.1016/0021-9290(72)90010-3.
[50] M.-G. Zhang, Y.-P. Cao, G.-Y. Li, and X.-Q. Feng, “Spherical indentation method for determining the constitutive parameters of hyperelastic soft materials,” *Biomech Model Mechanobiol*, vol. 13, no. 1, pp. 1–11, Jan. 2014, doi: 10.1007/s10237-013-0481-4.
[51] L. Dubuis, S. Avril, J. Debayle, and P. Badel, “Identification of the material parameters of soft tissues in the compressed leg,” *Computer Methods in Biomechanics and Biomedical Engineering*, vol. 15, no. 1, pp. 3–11, 2012, doi: 10.1080/10255842.2011.560666.
[52] F. Frauziols *et al.*, “In vivo Identification of the Passive Mechanical Properties of Deep Soft Tissues in the Human Leg,” *Strain*, vol. 52, no. 5, pp. 400–411, 2016, doi: 10.1111/str.12204.
[53] M. Petre, A. Erdemir, V. P. Panoskaltsis, T. A. Spirka, and P. R. Cavanagh, “Optimization of nonlinear hyperelastic coefficients for foot tissues using a magnetic resonance imaging deformation experiment,” *Journal of Biomechanical Engineering*, vol. 135, no. 6, pp. 61001–61012, Jun. 2013, doi: 10.1115/1.4023695.
[54] T. P. Babarenda Gamage, V. Rajagopal, M. Ehrgott, M. P. Nash, and P. M. F. Nielsen, “Identification of mechanical properties of heterogeneous soft bodies using gravity loading,” *International Journal for Numerical Methods in Biomedical Engineering*, vol. 27, no. 3, pp. 391–407, Mar. 2011, doi: 10.1002/cnm.1429.
[55] S. Evans and S. Avril, “Identification of material parameters through inverse finite element modelling,” *Computer Methods in Biomechanics and Biomedical Engineering*, vol. 15, no. 1, pp. 1–2, 2012, doi: 10.1080/10255842.2012.650321.
[56] S. L. Evans and C. A. Holt, “Measuring the mechanical properties of human skin *in vivo* using digital image correlation and finite element modelling,” *The Journal of Strain Analysis for Engineering Design*, vol. 44, no. 5, pp. 337–345, 2009, doi: 10.1243/03093247JSA488.
[57] S. Hartmann and R. R. Gilbert, “Identifiability of material parameters in solid mechanics,” *Archive of Applied Mechanics*, vol. 88, no. 1–2, pp. 3–26, Feb. 2018, doi: 10.1007/s00419-017-1259-4.
[58] R. Mahnken, “Identification of Material Parameters for Constitutive Equations,” in *Encyclopedia of Computational Mechanics*, E. Stein, R. de Borst, and T. J. R. Hughes, Eds. Chichester, UK: John Wiley & Sons, Ltd, 2004, p. ecm043. doi: 10.1002/0470091355.ecm043.
[59] B. N. Safa, M. H. Santare, C. R. Ethier, D. M. Elliott, E. C. Ross, and D. M. Elliott, “Identifiability of tissue material parameters from uniaxial tests using multi-start optimization,” *Acta Biomaterialia*, vol. 123, pp. 197–207, Mar. 2021, doi: 10.1016/J.ACTBIO.2021.01.006.
[60] K. Genovese, L. Casaletto, J. D. Humphrey, and J. Lu, “Digital image correlation-based point-wise inverse characterization of heterogeneous material properties of gallbladder in vitro,” *Proceedings of the Royal Society A: Mathematical, Physical and Engineering Sciences*, vol. 470, no. 2167, pp. 20140152–20140152, 2014, doi: 10.1098/rspa.2014.0152.

[61] M. Palanca, G. Tozzi, and L. Cristofolini, "The use of digital image correlation in the biomechanical area: a review," *International Biomechanics*, vol. 3, no. 1, pp. 1–21, 2016, doi: 10.1080/23335432.2015.1117395.
[62] B. Chen, K. Genovese, and B. Pan, "In vivo panoramic human skin shape and deformation measurement using mirror-assisted multi-view digital image correlation," *Journal of the Mechanical Behavior of Biomedical Materials*, vol. 110, p. 103936, Oct. 2020, doi: 10.1016/j.jmbbm.2020.103936.
[63] D. Solav, K. M. Moerman, A. M. Jaeger, and H. M. Herr, "A Framework for Measuring the Time-Varying Shape and Full-Field Deformation of Residual Limbs Using 3-D Digital Image Correlation," *IEEE Transactions on Biomedical Engineering*, vol. 66, no. 10, pp. 2740–2752, Oct. 2019, doi: 10.1109/tbme.2019.2895283.
[64] D. Solav, K. M. Moerman, A. M. Jaeger, K. Genovese, and H. M. Herr, "MultiDIC: an Open-Source Toolbox for Multi-View 3D Digital Image Correlation," *IEEE Access*, vol. 6, pp. 30520–30535, May 2018, doi: 10.1109/ACCESS.2018.2843725.
[65] K. M. Moerman, C. A. Holt, S. L. Evans, and C. K. Simms, "Digital image correlation and finite element modelling as a method to determine mechanical properties of human soft tissue in vivo," *Journal of Biomechanics*, vol. 42, no. 8, pp. 1150–1153, 2009, doi: 10.1016/j.jbiomech.2009.02.016.
[66] L. Han, J. A. Noble, and M. Burcher, "A novel ultrasound indentation system for measuring biomechanical properties of in vivo soft tissue," *Ultrasound in Medicine and Biology*, vol. 29, no. 6, pp. 813–823, Jun. 2003, doi: 10.1016/S0301-5629(02)00776-7.
[67] B. J. Ranger, K. M. Moerman, B. W. Anthony, and H. M. Herr, "Constitutive parameter identification of transtibial residual limb soft tissue using ultrasound indentation and shear wave elastography," *Journal of the Mechanical Behavior of Biomedical Materials*, p. 105541, Oct. 2022, doi: 10.1016/j.jmbbm.2022.105541.
[68] P. E. Chatzistergos, S. Behforootan, D. Allan, R. Naemi, and N. Chockalingam, "Shear wave elastography can assess the in-vivo nonlinear mechanical behavior of heel-pad," *Journal of Biomechanics*, vol. 80, pp. 144–150, Oct. 2018, doi: 10.1016/j.jbiomech.2018.09.003.
[69] J. Dong and W.-N. Lee, "Noninvasive Assessment of In Vivo Passive Skeletal Muscle Mechanics as a Composite Material Using Biomedical Ultrasound," *IEEE Transactions on Biomedical Engineering*, vol. 69, no. 3, pp. 1162–1172, Mar. 2022, doi: 10.1109/TBME.2021.3115144.
[70] K. M. Moerman, A. M. J. Sprengers, A. J. Nederveen, and C. K. Simms, "A novel MRI compatible soft tissue indentor and fibre Bragg grating force sensor," *Medical Engineering & Physics*, vol. 35, no. 4, pp. 486–499, Apr. 2013, doi: 10.1016/j.medengphy.2012.06.014.
[71] S. A. Maas, B. J. Ellis, G. A. Ateshian, and J. A. Weiss, "FEBio: Finite elements for biomechanics," *Journal of Biomechanical Engineering*, vol. 134, no. 1, p. 011005, Jan. 2012, doi: 10.1115/1.4005694.
[72] K. M. Moerman, "GIBBON: The Geometry and Image-Based Bioengineering add-On," *The Journal of Open Source Software*, vol. 3, no. 22, p. 506, 2018, doi: 10.21105/joss.00506.
[73] B. K. Zimmerman and G. A. Ateshian, "A Surface-to-Surface Finite Element Algorithm for Large Deformation Frictional Contact in febio," *Journal of Biomechanical Engineering*, vol. 140, no. 8, Aug. 2018, doi: 10.1115/1.4040497.
[74] S. S. Mirjavadi, A. J. Taberner, M. P. Nash, and P. M. F. Nielsen, "Characterising the Soft Tissue Mechanical Properties of the Lower Limb of a Below-Knee Amputee: A Review," in *Computational Biomechanics for Medicine*, Cham: Springer, Cham, 2021, pp. 99–111. doi: 10.1007/978-3-030-70123-9_8.
[75] C. Wex, S. Arndt, A. Stoll, C. Bruns, and Y. Kupriyanova, "Isotropic incompressible hyperelastic models for modelling the mechanical behaviour of biological tissues: a review," *Biomedical Engineering / Biomedizinische Technik*, vol. 60, no. 6, pp. 577–592, Dec. 2015, doi: 10.1515/bmt-2014-0146.
[76] K. M. Moerman, C. K. Simms, and T. Nagel, "Control of tension-compression asymmetry in Ogden hyperelasticity with application to soft tissue modelling," *Journal of the Mechanical Behavior of Biomedical Materials*, vol. 56, pp. 218–228, Mar. 2016, doi: 10.1016/j.jmbbm.2015.11.027.
[77] Y. Lanir, O. Lichtenstein, and O. Imanuel, "Optimal Design of Biaxial Tests for Structural Material Characterization of Flat Tissues," *Journal of Biomechanical Engineering*, vol. 118, no. 1, pp. 41–47, Feb. 1996, doi: 10.1115/1.2795944.
[78] M. H. Nathanson and G. M. Saidel, "Multiple-objective criteria for optimal experimental design: application to ferrokinetics," *American Journal of Physiology-Regulatory, Integrative and Comparative Physiology*, vol. 248, no. 3, pp. R378–R386, 1985.
[79] G. Balaban, M. S. Alnæs, J. Sundnes, and M. E. Rognes, "Adjoint multi-start-based estimation of cardiac hyperelastic material parameters using shear data," *Biomech Model Mechanobiol*, vol. 15, no. 6, pp. 1509–1521, Dec. 2016, doi: 10.1007/s10237-016-0780-7.
[80] Z. Chen, T. Scheffer, H. Seibert, and S. Diebels, "Macroindentation of a soft polymer: Identification of hyperelasticity and validation by uni/biaxial tensile tests," *Mechanics of Materials*, vol. 64, pp. 111–127, Sep. 2013, doi: 10.1016/j.mechmat.2013.05.003.